JGR

RESEARCH ARTICLE

Key Points:
- About 80% of slip on the LVF in the seismogenic depth range is aseismic
- Seismic slip during the 2003 earthquake occurred on a previously locked patch
- Aseismic afterslip occurred around the area that ruptured seismically

Supporting Information:
- Readme
- Text S1 and Figures S1–S21

Correspondence to:
M. Y. Thomas,
marion.caltech@gmail.com

Spatiotemporal evolution of seismic and aseismic slip on the Longitudinal Valley Fault, Taiwan

Marion Y. Thomas[1], Jean-Philippe Avouac[1], Johann Champenois[2], Jian-Cheng Lee[3], and Long-Chen Kuo[3]

[1]Department of Geological and Planetary Sciences, California Institute of Technology, Pasadena, California, USA, [2]CNES, Paris, France, [3]Institute of Earth Sciences, Academia Sinica, Taipei, Taiwan

Abstract The Longitudinal Valley Fault (LVF) in eastern Taiwan is a high slip rate fault (about 5 cm/yr), which exhibits both seismic and aseismic slip. Deformation of anthropogenic features shows that aseismic creep accounts for a significant fraction of fault slip near the surface, whereas a fraction of the slip is also seismic, since this fault has produced large earthquakes with five $M_w > 6.8$ events in 1951 and 2003. In this study, we analyze a dense set of geodetic and seismological data around the LVF, including campaign mode Global Positioning System(GPS) measurements, time series of daily solutions for continuous GPS stations (cGPS), leveling data, and accelerometric records of the 2003 Chenkung earthquake. To enhance the spatial resolution provided by these data, we complement them with interferometric synthetic aperture radar (InSAR) measurements produced from a series of Advanced Land Observing Satellite images processed using a persistent scatterer technique. The combined data set covers the entire LVF and spans the period from 1992 to 2010. We invert this data to infer the temporal evolution of fault slip at depth using the Principal Component Analysis-based Inversion Method. This technique allows the joint inversion of diverse data, taking the advantage of the spatial resolution given by the InSAR measurements and the temporal resolution afforded by the cGPS data. We find that (1) seismic slip during the 2003 Chengkung earthquake occurred on a fault patch which had remained partially locked in the interseismic period, (2) the seismic rupture propagated partially into a zone of shallow aseismic interseismic creep but failed to reach the surface, and (3) that aseismic afterslip occurred around the area that ruptured seismically. We find consistency between geodetic and seismological constraints on the partitioning between seismic and aseismic creep. About 80–90% of slip on the southern section of LVF in the 0–26 km, seismogenic depth range, is actually aseismic. We infer that the clay-rich Lichi Mélange is the key factor promoting aseismic creep at shallow depth.

1. Introduction

Fault slip can be either aseismic or seismic. Geodetic techniques, combined with seismology, provide the tools to quantify the partitioning between these two modes of slip and to investigate the various factors that control their spatial and temporal variations. A number of subduction zone studies have exhibited spatiotemporal variations in the mode of slip in the 0–50 km seismogenic depth range: fault slip might be dominantly aseismic at places, as a result of steady creep in the interseismic period or transient afterslip following large earthquakes, and dominantly seismic at others [e.g., *Heki et al.*, 1997; *Freymueller et al.*, 2000; *Wallace et al.*, 2004; *Cross and Freymueller*, 2007; *Fournier and Freymueller*, 2007; *Chlieh et al.*, 2008; *Perfettini et al.*, 2010; *Loveless and Meade*, 2011; *Miyazaki et al.*, 2011; *Hsu et al.*, 2006; *Evans et al.*, 2012; *Ozawa et al.*, 2012; *Pritchard and Simons*, 2006]. Similarly, strong spatial variations of slip mode have been documented on some continental faults [*Burgmann et al.*, 2000; *Titus et al.*, 2006; *Murray et al.*, 2001; *Jolivet et al.*, 2012; *Kaneko et al.*, 2013]. However, how the partitioning between seismic and aseismic slip varies in time and space and what are the factors governing this behavior (such as temperature, lithology, and pore fluids) remain poorly understood questions. What controls the mode of slip is an important issue in seismotectonics, since the seismic potential of any fault strongly depends on the partitioning between seismic and aseismic slip.

Here we focus on the spatiotemporal evolution of slip on the Longitudinal Valley Fault (Figure 1). This fault runs parallel to the east coast of Taiwan and marks the suture zone between the continental margin of south China and the Luzon Arc on the Philippine Sea Plate [*Lee et al.*, 2001; *Chang et al.*, 2009] (Figures 1a and 2). The Longitudinal Valley Fault (LVF) is known to creep near the surface [*Angelier et al.*, 1997; *Lee et al.*,
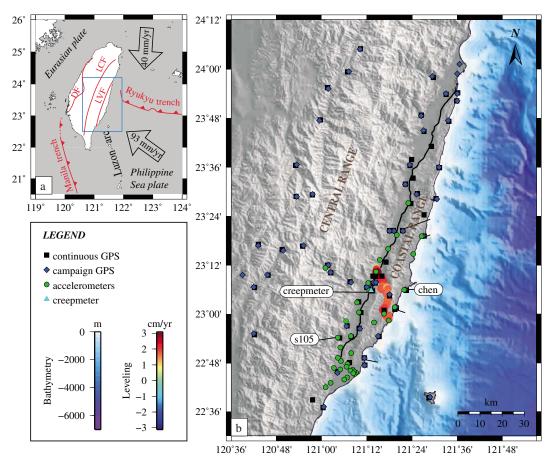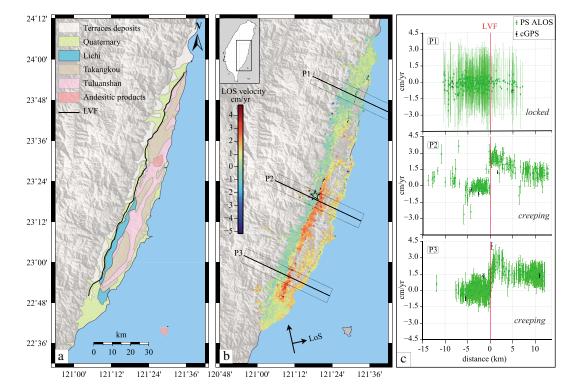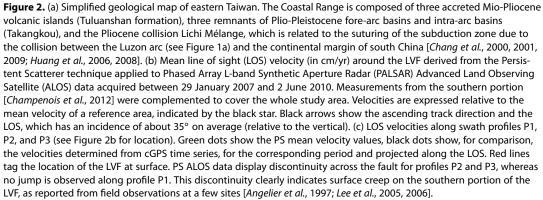
Figure 1. (a) Regional tectonic setting of the Longitudinal Valley Fault. Blue rectangle corresponds to the location of Figure 1b. DF: deformation front; LCF: Lishan-Chaochou Fault; and LVF: Longitudinal Valley Fault. (b) Location of accelerometric, geodetic, and leveling data used in this study. Black squares, blue diamonds, green circles, and cyan triangle stand for the 67 permanent GPS stations (http://gps.earth.sinica.edu.tw/), the 38 accelerometers [*Wu et al.*, 2006a], the 45 campaign GPS sites [*Yu and Kuo*, 2001], and the creepmeter [*Chang et al.*, 2009; *Lee et al.*, 2005], respectively. We labeled the stations corresponding to the time series shown in Figure 3. Colored-scale circles show the location of leveling measurements from 1 September 2007 to 31/10/2010 [*Chen et al.*, 2012].

1998, 2000, 2001, 2005; *Chang et al.*, 2009; *Champenois et al.*, 2012] but has also produced $M_w > 6.8$ earthquakes, including four events in 1951 [*Shyu et al.*, 2007], and the M_w 6.8 Chengkung earthquake of 2003 [*Wu et al.*, 2006a; *Hsu et al.*, 2009a; *Mozziconacci et al.*, 2009]. In addition, the surface strain is well documented from campaign mode GPS [*Yu and Kuo*, 2001], continuously recording GPS stations (cGPS) of the Taiwan Earthquake center (http://gps.earth.sinica.edu.tw/), leveling data [*Ching et al.*, 2011; *Chen et al.*, 2012], creepmeters [*Lee et al.*, 2001, 2005; *Chang et al.*, 2009], and interferometric synthetic aperture radar (InSAR) [*Hsu and Burgmann*, 2006; *Peyret et al.*, 2011; *Champenois et al.*, 2012]. Finally, the slip rate on the Longitudinal Valley Fault is extremely fast, absorbing nearly half of the 9 cm/yr horizontal convergence rate between the Philippine Sea Plate and south China [*Lee and Angelier*, 1993; *Yu et al.*, 1997; *Hsu et al.*, 2003; *Shyu et al.*, 2006; *Huang et al.*, 2010](Figure 1).

Hereafter, we first describe the compilation of geodetic and remote sensing data enhanced with new InSAR measurements. This data set covers the period from 1992 to 2010. We then present modeling results, starting with the secular interseismic creep rates. We then discuss the coseismic slip distribution related to the Chengkung event, and finally we analyze the spatiotemporal variations of creep rates observed over the study period, in particular due to postseismic relaxation following the 2003 earthquake.

Figure 2. (a) Simplified geological map of eastern Taiwan. The Coastal Range is composed of three accreted Mio-Pliocene volcanic islands (Tuluanshan formation), three remnants of Plio-Pleistocene fore-arc basins and intra-arc basins (Takangkou), and the Pliocene collision Lichi Mélange, which is related to the suturing of the subduction zone due to the collision between the Luzon arc (see Figure 1a) and the continental margin of south China [*Chang et al.*, 2000, 2001, 2009; *Huang et al.*, 2006, 2008]. (b) Mean line of sight (LOS) velocity (in cm/yr) around the LVF derived from the Persistent Scatterer technique applied to Phased Array L-band Synthetic Aperture Radar (PALSAR) Advanced Land Observing Satellite (ALOS) data acquired between 29 January 2007 and 2 June 2010. Measurements from the southern portion [*Champenois et al.*, 2012] were complemented to cover the whole study area. Velocities are expressed relative to the mean velocity of a reference area, indicated by the black star. Black arrows show the ascending track direction and the LOS, which has an incidence of about 35° on average (relative to the vertical). (c) LOS velocities along swath profiles P1, P2, and P3 (see Figure 2b for location). Green dots show the PS mean velocity values, black dots show, for comparison, the velocities determined from cGPS time series, for the corresponding period and projected along the LOS. Red lines tag the location of the LVF at surface. PS ALOS data display discontinuity across the fault for profiles P2 and P3, whereas no jump is observed along profile P1. This discontinuity clearly indicates surface creep on the southern portion of the LVF, as reported from field observations at a few sites [*Angelier et al.*, 1997; *Lee et al.*, 2005, 2006].

2. Data Used in This Study

We assembled all available data on geodetic surface strain (Figures 1 and 2) to invert for spatiotemporal variations of fault slip. We used data from continuously recording GPS stations, installed by the Central Weather Bureau, the Institute of Earth Sciences of Academia Sinica, the National Taiwan University, the Ministry of Interior, the Hualien County Government, and the National Land Surveying and mapping center (http://gps.earth.sinica.edu.tw/). We augment this data set with data from the literature, including campaign GPS data [*Yu and Kuo*, 2001], accelerometric data [*Wu et al.*, 2006a], time series of creepmeter measurements [*Lee et al.*, 2000, 2001, 2003, 2005; *Chang et al.*, 2009], leveling data [*Chen et al.*, 2012; *Ching et al.*, 2011], and the mean ground velocities measured from the Persistent Scatterer technique (PS) applied to Phased Array L-band Synthetic Aperture Radar (PALSAR) ALOS images covering the 2007–2010 period [*Champenois et al.*, 2012]. The PS data derived from ALOS images cover the southern half of the Longitudinal Valley. We extended the existing SAR data set with new measurements so as to cover the northern portion of the Longitudinal Valley [*Champenois*, 2011]. The following subsections describe these various data in greater detail.

There is also a leveling data set covering the whole island of Taiwan over the time period of 2000–2008 [*Ching et al.*, 2011]. We use this data set to check the consistency with the cumulative vertical displacements predicted by our model (see Figure S20).

2.1. PS Mean Velocities From the ALOS PALSAR Data Set

We used L-band PALSAR images (23.6 cm) provided by the ALOS satellite from the Japan Aerospace Exploration Agency to enhance the spatial resolution afforded by the GPS and leveling data, and we supplement the results of *Champenois et al.* [2012] obtained on the southern portion of the Longitudinal Valley to achieve a full coverage of the study area [*Champenois*, 2011]. We processed a 3 year long time series, from 12 January 2007 to 7 September 2010, using the Persistent Scatterer (PS) approach [*Ferretti et al.*, 2001; *Hooper et al.*, 2007]. The data set consists of 12 SAR images, which were acquired along the ascending path 444 every 3 months on average, except for a notable 9 month gap between January 2008 and October 2008. Because of the strong tropospheric effects altering the time series, we used these data to determine the mean line of sight (LOS) velocity over the time period 12 January 2007 to 7 September 2010 . Interferograms were generated using ROI_PAC [*Rosen et al.*, 2004] with the 17 October 2008 acquisition chosen as the master image and a 40 m horizontal resolution digital elevation model (DEM) for topographic corrections (this national DEM was derived from aerial photogrammetry). We then applied the Stanford Method for Persistent Scatterers (StaMPSs) [*Hooper et al.*, 2007]. StaMPS uses both amplitude dispersion and phase stability to determine the pixels, which can be considered as PS. No a priori model of deformation is required; nevertheless, it assumes that deformation, and consequently the interferometric phase, is spatially correlated. The technique yielded a total of 147,737 PS with a density of about 120–140 PS per km^2. StaMPS allows for estimation of the mean ground velocities averaged over the time period covered by the time series, projected along LOS of the satellite, at the location of each PS. Results are displayed in Figure 2. Mean velocities were computed with respect to a reference area, corresponding to the city of Rueisuei, near Yuli (black star on the map). Uncertainties estimated through the StaMPS method are of the order of 3–4 mm/yr on average.

The highest density of PS was retrieved in urban areas, in particular within the two largest cities in the Longitudinal Valley, Hualien in the North and Taitung in the South. For the same reason, we observe a greater density of PS inside the valley, where urbanization is the most developed, whereas PS are sparser in the Coastal Range, and mostly absent in the Central Range. The rugged topography and dense vegetation are most likely the reason for a lack of PS in those areas. The map of LOS velocities (positive toward the satellite) retrieved from this study shows a clear step in the velocity field along the LVF, south of 23°30 (Figure 2). This discontinuity is clear evidence of aseismic slip near the surface for the southern portion of the LVF. This observation is consistent with previously reported field observations of creep at a few sites [*Angelier et al.*, 1997; *Lee et al.*, 2005, 2006] and former InSAR studies [*Hsu and Burgmann*, 2006; *Peyret et al.*, 2011; *Champenois et al.*, 2012]. We took advantage of the great spatial resolution to better define the surface trace of the fault in the south. In the north, the ALOS PS measurements span the fault trace mapped by [*Shyu et al.*, 2005] but show no clear discontinuity (at the detection level of the technique, which we estimate to about 2 mm/yr at the 67% confidence level), suggesting the shallow portion of the fault has remained locked over the 2007–2010 period. This is consistent with the fact that, to our knowledge, there is no evidence for surface creep along the northern section of the LVF reported in the literature.

2.2. Continuous GPS Stations

For the purpose of this study, we used cGPS time series data from 67 stations spanning the Longitudinal Valley, the Coastal Range, the western part of the Central Range and Ludao Island (Figure 1) (http://gps.earth.sinica.edu.tw/). The time series starts on 1 January 1994 for the earliest stations, and we analyzed data collected until 26 November 2010 (Figure 3). The stations are equipped with dual-frequency geodetic GPS receivers136 (Trimble 4000 SST Geodetic II P and 4000 SSE/SSI Geodetic Surveyor). The sampling interval for data logging is 15 s. The data were processed by the GPS Lab at the Institute of Earth Sciences (Academia Sinica) using the Bernese (5.0) software package. The daily regional solutions are combined with solutions for five global International Global Navigation Satellite Systems Service networks provided by Scripps Orbit Permanent Array Center (http://sopac.ucsd.edu/sites/) to yield daily station coordinates for all sites in the International Terrestrial Reference Frame (ITRF) 2000 realization [*Yu and Kuo*, 2001; *Kuo*, 2008]. The the GPS Lab website. They were next converted to ITRF2005 using the transformation parameters provide by ITRF (http://itrf.ensg.ign.fr/ITRF_solutions/).
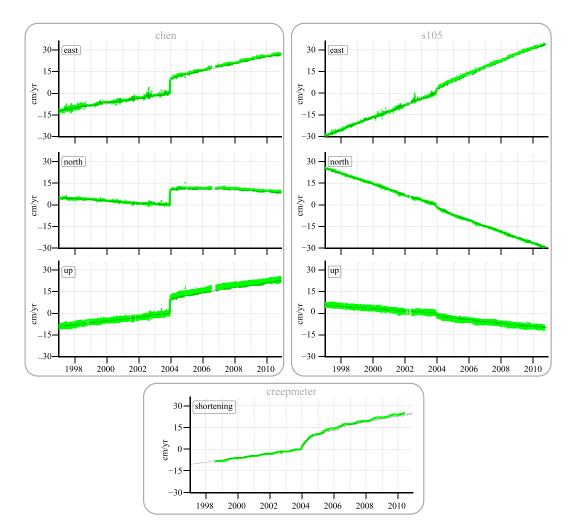
Figure 3. Plots of time series recorded at cGPS stations chen and s105 (http://gps.earth.sinica.edu.tw) and creepmeter measurements [*Chang et al.*, 2009; *Lee et al.*, 2005]. See Figure 1 for location. We show two stations with long time records and surrounding the coseismic and postseismic area. See supporting information for other time series (Figures S1–S3 in the supporting information). Green dots with 1 sigma error bars represent the original data set. Predictions from the inversion of coseismic slip and Principal Component Analysis-based Inversion Method (PCAIM) inversions of preseismic and postseismic periods are plotted in black. To facilitate the comparison we have corrected the model predictions for the mean residual velocities over the preseismic and postseismic period represented in Figures 12 and 14.

The dominant sources of signal over this time period are interseismic loading, coseismic, and postseismic displacements due to the 2003 M_w 6.8 Chenkung earthquake [*Chen et al.*, 2006; *Lee et al.*, 2006; *Wu et al.*, 2006a; *Ching et al.*, 2007; *Hu et al.*, 2007; *Kuochen et al.*, 2007; *Savage*, 2007; *Wu and Wu*, 2007; *Cheng et al.*, 2009; *Hsu et al.*, 2009a; *Huang et al.*, 2009; *Mozziconacci et al.*, 2009]. The southernmost stations in the Longitudinal Valley have also recorded displacements due to the 2006 M_w 6.1 Peinan earthquake [*Wu et al.*, 2006b; *Chen et al.*, 2009]. This earthquake did not take place on the LVF but on a fault bounding the Central Range [*Wu et al.*, 2006b; *Chen et al.*, 2009]. Therefore, for the purpose of this study, we corrected the GPS time series for the effect of the 2006 Peinan earthquake and its subsequent postseismic relaxation, by adopting the following functional form for the time series:

$$
\begin{aligned}
u^i(t) = u^i_0 + v^i t + \sum_k h^k_j \mathcal{H}(t - t_k) \\
+ \sum_k r^i_k \mathcal{H}(t - t_k) \log(1 + (t - t_k)/\tau) \\
+ \sum_p \left(s^i_p \sin\left(\frac{2\pi t}{T_p} \right) + c^i_p \cos\left(\frac{2\pi t}{T_p} \right) \right),
\end{aligned}
\tag{1}
$$

where i = (north, east, and up), u_0 is a constant offset, vt correspond to the secular velocity, $\mathcal{H}$ is a Heaviside step function standing for coseismic displacement, t_k is the time at which the step occurs, and the Heaviside step function multiplied by the logarithmic function follows the postseismic relaxation with τ, the characteristic time constant. We then must estimate the coefficients c_p and s_p to model the harmonic variations of period T_p. We consider annual and a semiannual periods. The linear parameters u_0^i, v^i, h_j^i, r_k^i, s_p^i, and c_p^i are estimated through a standard least squares inversion. Artificial steps due to maintenance operations, small local earthquakes, effect of far-field earthquakes (such as the 1999 Chichi earthquake [*Ma et al.*, 1999]) or equipment malfunction might also affect the signal. We removed them from the time series by applying the same process (equation (1)). We estimate the standard deviation on daily positions to be about 4 mm for the east and the north components and 16 mm for the vertical component, based on the residuals obtained from fitting the corrected time series with a linear regression (equation (1)). The linear regression to the time series would yield underestimated uncertainties on the secular velocities as it is incorrect to assume a purely white noise model [*Zhang et al.*, 1997; *Langbein and Johnson*, 1997; *Williams*, 2003]. The linear regression results are therefore used only to weight the relative contributions of the various data set in the determination of the best fitting fault slip models. The uncertainties are estimated a posteriori from normalization of the reduced chi-square criterion as detailed in section 3.2. Values are listed in Table 2.

2.3. Creepmeter Data

Creep on the Chihshang segment of the LVF has been measured daily over the last 15 years thanks to a network of creepmeters [*Lee et al.*, 2000, 2001, 2003, 2005; *Chang et al.*, 2009]. We used data from 26 July 1998 to 24 May 2010 from the three creepmeters installed at Chinyuan site (Figure 1) but did not include the records from the Tapo site because gravity-driven slumping is thought to interfere with fault slip at this site [*Lee et al.*, 2003]. Creepmeters have been set up across the three major splay faults within a 120 m wide deformation zone. Each creepmeter provides a scalar measurement of the horizontal shortening along the baseline of the instrument (N113°, N156°, and N164°). We projected and summed the time series along the direction of maximum shortening (N146°) defined by trilateration method and GPS interseismic vectors at the same site [*Angelier et al.*, 1997; *Lee et al.*, 2006].

No detectable coseismic slip occurred at the surface during the 2003 Chengkung earthquake. By contrast, accelerated creep (i.e., postseismic creep) was observed during the year following the event (Figure 3). All three creepmeters at Chinyuan site show strong seasonal variation of fault creep, with fast creep during wet season and quiescence during the dry season. This behavior is interpreted to result from pore pressure variations caused by rainfall, as suggested by the correlation with piezometric measurements in a local well [*Chang et al.*, 2009]. Based on the residuals obtained from fitting the time series with a linear regression (equation (1)), we estimate the uncertainty on the individual creepmeter measurements to be 2 mm at the 67% confidence level.

2.4. Campaign GPS Measurements and Secular Velocities Inferred From cGPS Time Series

Annual GPS surveys at 45 campaign sites were conducted across the Longitudinal Valley between 1992 and 1999 [*Yu and Kuo*, 2001] (Figure 1). Estimated uncertainties based on [*Yu and Kuo*, 2001] are 0.2 mm for the east and the north components and 0.4 mm for the vertical component. We supplemented this data set with the secular velocities (vt) at the continuous GPS stations, estimated from equation (1). The linear regeression would yield uncertainties of 0.1 mm/yr for the northern and eastern components and 0.5 mm/yr for the vertical. As discussed in section 2.2, the linear regression results are used to balance the relative contribution of the various data to the total misfit and the uncertainties are estimated a posteriori through normalization of the reduced chi-square criterion (Table 2).

2.5. Leveling Data

We used vertical displacements derived from a leveling survey in the southern part of the Coastal Range (Figure 1). Those measurements were acquired on an annual basis between 1 September 2007 and 31/10/2010 along a leveling line crossing the Chihshang segment of the Longitudinal Valley fault [*Chen et al.*, 2012]. We used these data to estimate the average vertical rates (relative to the first station along the leveling line) over the 1 September 2007 and 31/10/2010 period. Uncertainty varies from the initial reference point (0 mm) up to 19 mm for the last point.

2.6. Accelerometric Data

In order to constrain coseismic slip due to the 2003 M_w 6.8 Chengkung earthquake, we used the static displacements measured from the offsets in the cGPS records, together with the static displacements
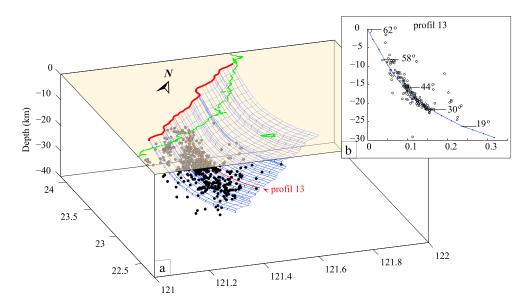
Figure 4. (a) Three-dimensional fault geometry (blue grid) determined from the surface fault trace (red line) and relocated seismicity(black dots) for events of $M_w \geq 2.5$ [*Wu et al.*, 2008b]. The geometry at depth is well constrained only in the Chengkung earthquake area due to the intense aftershock activity. (b) Profile shows the variation of dip angle with depth. Black dots corresponds to seismic events.

determined by *Wu et al.* [2006a; *Hu et al.*, 2007] from the accelerometric measurements recorded at 38 stations from the Taiwan Strong Motion Instrumentation Program (TSMIP) network (Figure 1). TSMIP stations, operating under low-gain mode, sample the signal at 200 Hz [*Wu et al.*, 2006a]. Uncertainties were inferred to be 2.9 mm for the horizontal components and 1.9 mm for the vertical [*Wu et al.*, 2006a].

3. Modeling Approach and Assumptions

3.1. Fault Geometry and the Forward Model

The data set presented above are used to estimate the time evolution of slip on the LVF. We assume that the medium surrounding the fault is behaving elastically and apply the *Okada* [1985] semianalytical solution to relate slip at depth to surface displacement. This solution assumes an elastic half-space. Heterogeneities of elastic properties and topographic effects are neglected.

We defined a 3-D fault geometry based on the location and depth of aftershocks of the Chengkung event [*Kuochen et al.*, 2007, *Wu et al.*, 2007, 2008a], and the surface trace of the LVF, determined from the discontinuity in the PS ALOS velocity field (Figure 2) and the geomorphologic expression of the fault for the northern part [*Shyu et al.*, 2005] (Figure 4). Both the relocated seismicity and the local tomographic results [*Kuochen et al.*, 2007; *Wu et al.*, 2007, 2008a] suggest that the LVF is a listric fault with a dip angle decreasing gradually from about 62° at shallow depth (0–14 m) to 19° at 27 km depth and thereafter. This geometry is relatively well constrained for the central and the southern portion of the LVF, because of the intense aftershock activity following the Chengkung earthquake. We assume that the same listric geometry holds for the northern portion of the LVF, although we have no direct constraints there. This fault is subdivided into 44 × 15 and 3.16 × 3.16 km patches. The fault extends over about 140 km along strike (the length of the longitudinal valley) and about 47 km along dip.

Assuming a linear purely elastic half-space, displacements at surface are related to the fault slip distribution through a Fredholm integral equation of the first kind, which, if we use *k* measurements and discretize the fault plane in *l* patches, gives in the matrix form

$$\mathbf{d} = \mathbf{Gm}, \tag{2}$$

where **d** is the input data vector, **G** is the $k \times l$ Green's functions matrix that relates slip at depth and surface displacements, and **m** is the vector of parameters we are solving for, i.e., strike-slip and dip-slip components of the slip vector. For an elastic half-space, the Green's functions depend on the Poisson ratio, which is fixed

to 0.25. The rigidity modulus is fixed to a standard value of 30 GPa and used only to convert slip potency (integral of slip over the fault area) to moment (expressed in N.m.).

3.2. Inversion Procedure

The slip distribution needed to account for the observed surface displacements, **d**, is solved through a standard linear inversion. In order to take into account the uncertainties on the measurements, we normalize the data using C_d, the data covariance matrix. This procedure allows for combining data with different noise characteristics, such as GPS and InSAR observations, with appropriate relative weighting. Equation (2) then becomes

$$\mathbf{C_d}^{-1}\mathbf{d} = \mathbf{d}^* = \mathbf{C_d}^{-1}\mathbf{Gm} = \mathbf{G}^*\mathbf{m}. \tag{3}$$

Solving equation (3) for the fault slip **m** minimizes the weighted Root Mean Square (RMS) of the difference between the observed and predicted displacement, with the weighting of each data point being determined by its uncertainty. It is equivalent to minimizing a reduced chi-square criterion defined as follows:

$$\chi_{red}^2(\mathbf{m}) = 1/n \parallel \mathbf{G}^*\mathbf{m} - \mathbf{d}^* \parallel^2, \tag{4}$$

where n is the number of data points. We imposed the reduced χ^2 to be equal to 1 when computed on each data set separately. These renormalization accounts for some sources of errors that are not properly taken into account in the a priori estimates of the uncertainties, such as those due to heterogeneities of the elastic medium or topography or due to the misestimate of a priori data uncertainties (Table 2).

However, the inversions described below are poorly constrained due to the large number of unknowns ($44 \times 15 = 1320$) and trade-offs among model parameters. To regularize the inversion, we impose the constraint that fault slip distribution be smooth. Following an approach suggested by *Lohman* [2004], we weigh the constraint put on smoothing according to local resolution of the inversion. Therefore, the fault slip is retrieved by minimizing some combination of the model's ability to fit the data and the penalty imposed on the roughness of the slip distribution, which is quantified from its Laplacian:

$$\phi_d = \parallel \mathbf{G}^*\mathbf{m} - \mathbf{d}^* \parallel^2 + \frac{1}{\lambda} \parallel \mathbf{S\Lambda m} \parallel^2, \tag{5}$$

where $\mathbf{\Lambda}$ is the Laplacian matrix, $\mathbf{S}$ is a diagonal smoothing shape matrix that weighs each row of $\mathbf{\Lambda}$, and λ defines the weight attributed to the penalty. $\mathbf{S}$ is defined as the inverse of the width of the best fitting Gaussian curve to each row of the resolution matrix (see supporting information from *Ader et al.* [2012] for details). Consequently, well-resolved patches have small or no smoothing applied, whereas poorly resolved regions are strongly smoothed.

Figures S4 and S5 (see supporting information) illustrate the resolution for the various inversions described below. The resolution is expressed here in terms of the characteristic size of the smallest inhomogeneities of coupling which could in principle be resolved, given the spatial distribution and the uncertainties of the measurements. For each case we take into account the distribution of data and their uncertainties and plot, at the location of each cell of the fault model, the width of the best fitting Gaussian curve to each row of the resolution matrix. In effect, this representation is equivalent to the width of the Gaussian distribution that is retrieved if one inverts the displacements predicted for a unit slip at the considered cell. These maps show that, past the coastline, the resolution on fault slip at depth becomes quite poor, as expected given the absence of any offshore constraints except for the cGPS station on Ludao Island (Figure 1). Features smaller than about 10 km cannot, in principle, be resolved there. Updip of the coastline the resolution is generally better than about 5 km.

To illustrate the resolution power of our inversions, we show in Figure 5 the result of the inversion of a synthetic source model. The input consists of a rectangular source with a uniform slip of 1 m. The location and size of the source was chosen so that this source is comparable to that of the 2003 M_w 6.8 earthquake. Synthetic displacements were computed at the locations of the GPS and accelerometric stations and were assigned the same uncertainties as the original observations. Inverted slip distribution from the synthetic data set emphasize the along-strike and along-dip variations of resolution for the coseismic model.
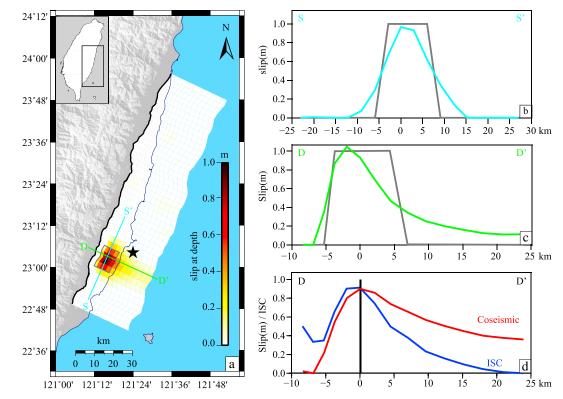
Figure 5. Resolution test. (a) The input is theoretical displacements computed for a rectangular source (black box) with a uniform slip of 1 m. Figure 5a displays the inverted slip distribution from this synthetic data set. (b and c) The input (grey) and inverted slip distribution (colored) along strike (SS′) and along dip (DD′), respectively. Locations of profiles are reported in the map view in Figure 5a. (d) The inverted slip distribution for the Chenkung earthquake (red) and the interseismic coupling (blue) along dip (DD′). Interseismic coupling and coseismic models are displayed in Figures 7 and 10, respectively. Comparison of Figure 5c and the coseismic slip distribution (red) in Figure 5d demonstrates that the lack of resolution of depth only explains partially the downdip extend of the coseismic rupture.

3.3. Block Model Correction

Before any inversion for fault slip rate with depth, the surface displacements must first be referred to a local reference frame. In effect, we need to determine the long-term motion of the Coastal Range and Central Range, which bound the Longitudinal Valley Fault to the east and west, respectively. As is customary in plate tectonics or continental deformation studies, we use the Euler pole formalism to describe the long-term motion of the Coastal Range (CoR) and Central Range (CeR) blocks. Given that all the GPS stations are close to the LVF, it is not possible to determine these Euler poles reliably without taking into account interseismic strain. We therefore first determine jointly the secular pattern of fault slip (time-averaged fault slip over the study period) and the Euler poles of the CeR and CoR blocks relative to ITRF2005 (section 4). Then we infer coseismic slip due to the Chenkung earthquake. Both the coseismic and secular interseismic models are determined simply from solving equation (5), in which **d** represents the surface displacements. To retrieve the temporal variations of fault slip for the period preceding and following the 2003 event, we used PCAIM [*Kositsky and Avouac*, 2010], explained in more detail in the supporting information (Text S1).

4. Secular Interseismic Model
4.1. Data Used

We determine in this section the secular model of fault slip rate on the LVF, in the interseismic period. This model represents the mean slip rate distribution needed to account for the secular geodetic strain determined with proper correction for coseismic and postseismic transients. For this purpose, we use GPS campaign measurements, leveling data, PS ALOS mean velocity, and secular velocities determined with the continuous GPS and the creepmeter's timeseries (as determined from the least squares fitting of the time series with equation (1)). The leveling and ALOS data sets were acquired more than 3 years after the 2003 Chengkung earthquake. The GPS and the creepmeter data suggest that postseismic relaxation was

Table 1. Location of Axis and Angular Rotation Rates of Euler Poles Used to Describe the Relative Motions of the Philippine Sea Plate (Ph), Central Range Block (CeR), and Coastal Range Block (CoR)

	Ph/ITRF	CeR/Ph	CeR/CoR	CoR/Ph
Latitude	47.1	32.15	−23.34	−19.42
Longitude	150.4	133.30	−54.93	−58.11
$\Omega(°/Myr)$	−0.9251	−2.1351	7.0154	−4.94

mostly over by this time. Therefore, these data are incorporated in the secular inversion, which significantly improves the spatial resolution. Uncertainties assigned to these data sets are displayed in Table 2.

4.2. Long-Term Slip Rate on the Longitudinal Valley Fault

In order to get a secular model of slip on the LVF, we need to evaluate the long-term motion of the CoR and CeR blocks. Evidence for active thrusting offshore the eastern coast of Taiwan [*Malavieille et al.*, 2002; *Huang et al.*, 2010] dismisses the CoR block as part of the Philippine Sea Plate. In addition, the Philippine Sea Plate motion is very poorly constrained as this plate is bounded only by subduction zones, and the few GPS sites on this plate might be affected by plate boundary strain. We therefore need to determine the secular motion of the CoR block. This requires us to take into account the interseismic strain associated with the LVF, since all the geodetic data are located less than ∼20 km away from the fault. Similarly, the CeR block is not fixed with respect to south China due to active thrusting along the western foothills of Taiwan [*Hsu et al.*, 2003], and none of the GPS data can reliably be considered to represent the long-term motion of the CeR block. The GPS stations are too close to the LVF to represent reliably the blocks motions. In such a situation it is customary to jointly invert for long-term block motion and the effect of locking of the bounding fault [e.g., *McCaffrey*, 2005; *Meade and Hager*, 2005]. We use a simple two-step procedure to evaluate the Euler poles, describing the long-term motion of these two blocks, with the Philippine Sea Plate chosen as a reference.

The point of the procedure is to estimate the Euler poles of the CeR and CoR with proper account for strain induced by interseismic locking on the LVF. In the first step, we estimate the CeR Euler pole using the secular velocities of the stations in the Central Range after correction for the strain induced by the pattern of interseismic creep on the LVF. To estimate the pattern of locking we use the stations east of the LVF only, in the precision spectral pyranometer (PSP)-fixed reference. In the second step, we calculate the Euler pole of the CoR after correcting the secular velocities for the strain induced by the pattern of interseismic creep on the LVF determined form the stations west of the LVF only. The patterns of interseismic creep derived at each step are similar and is next improved by combining the data from both sides of the fault. The risk of this iterative procedure is that the end result be biased by the choice of the initial PSP reference. We show in the supporting information the results obtained assuming a different initial Euler pole for the PSP (Figure S8). These tests, in which we change either the Philippine Sea Plate rotation rate by up to 25% or the location of the pole (starting with the pole of *Sella et al.* [2002] rather than the one of *DeMets et al.* [2011]), show that the procedure converges to the same solution. Therefore, we are confident that our results are not biased.

We first express the GPS velocities with respect to the Philippine Sea Plate by using the Euler pole (ITRF-Ph) computed by *DeMets et al.* [2011] (Table 1 and Figure 6). Then, using the back slip modeling approach [*Savage*, 1983], we invert for slip at depth using the campaign GPS data and the secular velocities derived from the continuous GPS time series, for stations east of the LVF. This model is then used to predict the GPS velocities at stations in the footwall (west of LVF) to further compare them with the secular velocities measured at those locations. If the LVF is assumed to be the only source of strain in the study area, then the residuals represent the long-term motion of the footwall with respect to the Philippine Sea Plate. Residuals for stations in the Central Range are then used to compute the Euler pole of the CeR block from a linear least squares inversion (CeR/Ph pole in Table 1 and Figure 6).

Next, we use the CeR/Ph Euler pole to express the secular velocities of the western stations in the local CeR reference frame. These data are now inverted for the coupling on the LVF using the back slip approach. Similarly to the previous step, we predict displacements at stations lying on the eastern side of the LVF and compute the residuals with the secular velocities at those sites, expressed in the CeR reference frame. We can now use these residuals to compute an Euler pole describing the motion of the CoR relative to CeR (see CeR/CoR pole in Table 1 and Figure 6). It is now possible to express the geodetic data in either the CeR or CoR reference frame and predict the long-term slip on the LVF fault needed to accommodate the relative block motion between the Central Range and Coastal Range (Figure S6 in the supporting
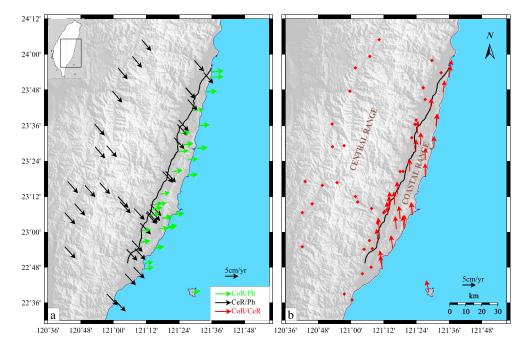
Figure 6. (a) Secular motion of the Central Range (black arrows) and Coastal Range (green arrows) blocks relative to the Philippine Sea Plate, as defined by Philippine/ITRF [*DeMets et al.*, 2011]. (b) Secular motion of the Coastal Range relative to the Central Range. Pole parameters are listed in Table 1.

information). The computation assumes that the blocks behave rigidly in the long term. This is only a first-order approximation, as the LVF is not strictly planar.

4.3. Secular Interseismic Slip and Interseismic Coupling on the LVF

We now use the complete data set of InSAR, GPS, and leveling measurements to determine the time-averaged pattern of slip rate on the LVF in the interseismic period. We assume that the deeper continuation of the fault is slipping at the long-term slip rate imposed by the relative block motion between the Central Range and Coastal Range, as predicted by the CeR/CoR Euler pole established in the previous section. Because of the very limited sensitivity of our data to slip at depth, we limit the inversion to the fault portion shallower than 26 km (corresponding to 15 cells of our gridded fault along the downdip direction). Consistently, for this model and the ones that follow, we only include in the inversion the GPS stations that could have recorded shallow slip displacement, i.e., stations that are at most ~30 km away from the fault trace.

We first predict the theoretical displacements at stations by assuming that the fault is fully locked from the surface to a depth of 26 km. To compute such a model we use again the back slip approach [*Savage*, 1983]. The CeR/CoR Euler pole characterizes the long-term surface velocities, and the back slip model is added to account for locking of the LVF down to 26 km depth. We then subtract the velocities predicted by this model from the measured velocities. These residuals must contain the signal due to creep on the LVF. We can now invert the residuals to get the spatial variation of secular slip rate on the LVF in the 0–26 km depth range of our model. We apply this procedure to all the data, including continuous and campaign GPS data, leveling measurements, and PS ALOS mean velocities.

The slip rate distribution obtained from this inversion and the comparison between the model predictions and the observations are plotted in Figures 7a, 8, 9, and S7 (in the supporting information). This model highlights the distinction between sections of the fault that are creeping and the ones that remain locked. As previously recognized, the southern portion of the fault is creeping near the surface [*Angelier et al.*, 1997; *Lee et al.*, 2000, 2001, 2003, 2005; *Hsu and Burgmann*, 2006; *Lee et al.*, 2006; *Chang et al.*, 2009; *Cheng et al.*, 2009; *Hsu et al.*, 2009b; *Huang et al.*, 2010; *Peyret et al.*, 2011; *Champenois et al.*, 2012; *Chen et al.*, 2012; *Chuang et al.*, 2012]. Our study highlights that, on the contrary, the northern part is mostly locked. The pattern at depth is more complex, with areas creeping at high rate, connecting the deeper and the upper part, while others
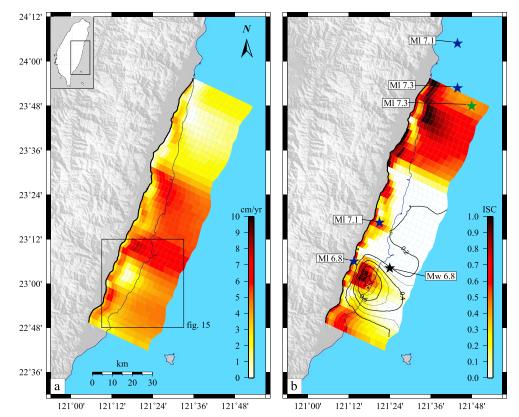
Figure 7. Secular interseismic model. (a) Slip rate distribution derived from the inversion of campaign GPS data, secular interseismic velocities inferred at cGPS stations, creepmeter secular rate, leveling data and PS ALOS mean velocities. The black rectangle shows locations of the map view displayed in Figure 15. (b) Interseismic coupling (ISC) distribution derived from the interseismic slip rate distribution shown in Figure 7a. ISC quantifies the degrees of locking of the LVF fault. If ISC = 1, then the fault patch is fully locked, whereas ISC = 0 means that the patch is creeping at the long-term slip rate. Black, green, and blue stars indicate the epicenter of the 2003 Chengkung earthquake, the 1938 earthquake, and the 1951 earthquakes sequence, respectively [*Chung et al.*, 2008]. Black curves show contour lines of coseismic slip distribution for the 2003 M_w 6.8 Chengkung Earthquake (Figure 10).

seem to be locked or partially locked. Moreover, epicenters of historical earthquakes on the LVF (1938, 1951, and 2003) [*Chung et al.*, 2008] seem to correlate with the location of partially locked patches (Figure 7b).

We can next estimate the interseismic coupling (ISC), which quantifies the degrees of locking of the fault. ISC is defined as the ratio of slip deficit divided by the long-term slip rate.

$$\text{ISC} = 1 - \frac{V_{\text{int}}(x)}{V_{\text{pl}}(x)}, \tag{6}$$

where V_{pl} is the long-term slip rate on the fault and V_{int} is the slip rate during the interseismic period. In principle, if no transient events occur during the time period considered to compute V_{int}, ISC values should be between 0 and 1. If ISC = 1, then the fault patch is fully locked, accumulating stress to be released during transient slip events (earthquakes or aseismic slow slip events, for example). If ISC = 0, then the patch is creeping at long-term slip rate. To compute the ISC on the LVF we divide the slip rates derived from the inversion of surface strain with the long-term slip rate predicted by the CeR/CoR Euler pole (Figure S6 in the supporting information). The inferred distribution of ISC is displayed in Figure 7b.

5. Source Model of the 2003 Chengkung Earthquake

We present here our determination of the slip distribution related to the Chengkung earthquake. This event, which occurred on 10 December 2003, ruptured the southern portion of the LVF. Several source models have already been established with different assumptions regarding the fault geometry or elastic structure [*Wu et al.*, 2006a; *Ching et al.*, 2007; *Hu et al.*, 2007; *Mozziconacci et al.*, 2009; *Cheng et al.*, 2009; *Hsu et al.*, 2009a]. We produce our own model to allow for a consistent comparison with interseismic and postseismic slip models.
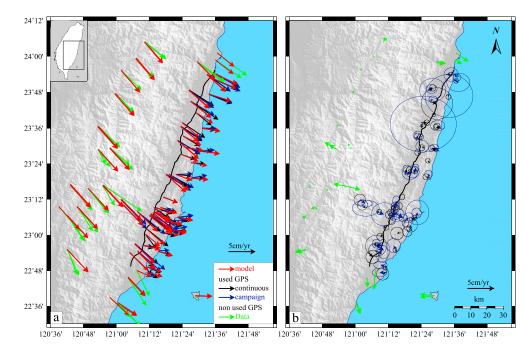
Figure 8. Interseismic coupling model, fit to geodetic data. (a) Comparison between observed and predicted horizontal velocities. The reference frame is the Philippine Sea Plate. The GPS data used in this inversion are plotted respectively as dark blue and black arrows for the campaign and continuous GPS measurements. Green arrows stand for the GPS stations that were not used in the inversion but which are plotted for reference. Predictions from the interseismic coupling model are displayed in red. (b) Residuals from the inversion with corresponding error ellipses. Same color attributions as in Figure 8a.

Coseismic slip on the LVF is determined based on the estimate of static displacements derived from the cGPS (33 sites) and accelerometric (38 sites) records [*Wu et al.*, 2006a; *Wu and Wu*, 2007; *Hu et al.*, 2007]. The coseismic displacements and the associated uncertainties at the cGPS stations are derived from the least squares fit to the time series using equation (1). The 1 sigma uncertainties are of the order of 1 mm and 4 mm for the horizontal and vertical components, respectively. With regard to the coseismic displacements retrieved from the accelerometric records, we initially use the uncertainties estimated by *Wu et al.* [2006a], which are reported to be 2.9 mm for the horizontal components and 1.9 mm for the vertical. Fault slip is determined from a standard least squares inversion of these data, as described in section 3.

In equation (5) λ is chosen to offer the best compromise between smoothness and fit to the data, which leads to $1/\lambda = 0.005$; for more details see Figure S9 in the supporting information, which plots the variation of χ^2 against λ. Uncertainties are renormalized to balance the relative contribution of the accelerometric and GPS data. We imposed the reduced χ^2 to be equal to 1 when computed on each data set separately, i.e., accelerometric uncertainties must be multiplied by 4.8, whereas uncertainties for inferred coseismic jumps from GPS time series must multiplied by 6.6. These renormalization factors suggest that some sources of errors are not properly taken into account in the initial estimates of the uncertainties. The renormalized uncertainties seem reasonable (of the order of a few millimeters, see Table 2).

Our coseismic model (Figures 10 and S10 in the supporting information) is in good agreement with previously published geodetic inversions [*Ching et al.*, 2007; *Hu et al.*, 2007; *Mozziconacci et al.*, 2009; *Cheng et al.*, 2009; *Hsu et al.*, 2009a] but somewhat smoother than the kinematic model of *Mozziconacci et al.* [2009], which incorporates GPS data as well as teleseismic and accelerometric waveforms. According to our model most of the slip occurred on a 10 × 10 km patch with a peak slip of 0.91 m at 17 km depth (Figure 10). The location of the rupture area is close to what *Mozziconacci et al.* [2009] obtained. Their source is more compact with a peak slip twice as large, probably because of the enhanced resolution afforded by the seismic waveforms (in such a joint inversions the static displacements constrain essentially the final slip distribution, while the waveforms provide constraint on the time history of slip). Our model shows no significant slip near the surface (Figure 10). This finding is in agreement with field observations and the absence of coseismic
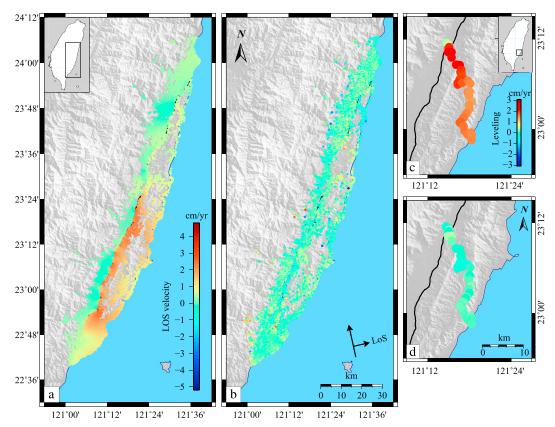
Figure 9. Interseismic coupling model, fit to PS ALOS mean velocity and leveling data. (a) Line of sight velocities predicted from the secular interseismic model. For comparison with observations see Figure 2. (b) Residuals from the inversion with same color scale as in Figure 9a. (c) Vertical velocities predicted from the secular interseismic model. See Figure 1 for corresponding observations. (d) Residuals from the inversion with same color scale as in Figure 9c.

offset in the creepmeter record, which is located updip of the zone with maximum slip. A few patches display 0.1 to 0.3 m of fault slip, but most of them show a displacement lower than 0.1 m.

The equivalent seismic moment released (M_0) was computed as the sum of the seismic moment of all individual subfaults, assuming a shear modulus ,μ, of 30 GPa:

$$M_0 = \mu \sum_i S_i \Delta u_i, \tag{7}$$

where S_i is the area of the subfault and Δu_i is the computed slip on S_i. Our model estimates the seismic moment to be 1.87×10^{19} N m, in close agreement with the moment of 2.07×10^{19} N m determined by *Mozziconacci et al.* [2009], assuming a shear modulus of 32 GPa. The equivalent moment Magnitude ($M_w = 6.8$), estimated using *Hanks and Kanamori* [1979] relation,

$$M_w = \frac{2}{3} \left(\log_{10} M_0 - 9.1 \right), \tag{8}$$

is consistent with the value reported in the Harvard-centroid moment tensor catalog.

6. Preseismic and Postseismic Temporal Variation of Fault Slip Rate

6.1. Inversion Procedure

We now determine the temporal variation of slip at depth before and after the 2003 Chenkung earthquake from modeling the geodetic time series. We use the PCAIM technique [*Kositsky and Avouac*, 2010], since this method has been designed to deal with temporal variations of fault slip and to allow simultaneous integration of different kinds of geodetic measurements and remote sensing data (see also *Lin et al.* [2010]; *Perfettini et al.* [2010]; *Wiseman et al.* [2011]; *Copley et al.* [2012] for examples of applications of that technique). The method is computationally cheap and allows us to take advantage of the spatial resolution

Table 2. Root Mean Square (RMS) and Normalization Factors (k) Times the Uncertainties (σ) Associated With the Various Data Sets Used in This Study (Given at the 67% Confidence Level)

$1/\lambda$	Secular 0.1		Coseismic 0.005		Postseismic 0.04		Preseismic 0.06	
	$k \times \sigma$	RMS	$k \times \sigma$	RMS	$k \times \sigma$	RMS	$k \times \sigma$	RMS
ALOS (mm/yr)	17.5	3.8			35	3.0		
Secular velocity (mm/yr)	6	4.9						
cGPS (mm)			6.6	6.7	1.2	6.5	1.4	10.3
Creepmeter (mm)					0.6	2.2	0.4	1.8
Campaign GPS (mm/yr)	8	2.6					1.8	9.0
Leveling[a] (mm/yr)	0 to 3.2	2.6			0 to 74	3.3		
Accelerometers (mm)			4.8	12.5				

[a]Leveling data are referred to the initial point in the survey. The uncertainty of elevation change measurement increases linearly as a function of distance from this point.

afforded by the remote sensing data, which are sparse in time but dense in space, together with the temporal resolution of the GPS time series which are sparse in space but dense in time. Details about the method are explained in the supporting information (Text S1).

A data set very sparse in time, such as the PS-ALOS data or the campaign GPS data, cannot be incorporated in the principal component analysis (PCA) decomposition but can be used to place constraints on the inversion of the principal components. The set of linear equation (Figure S4), considering only the meaningful components, is then inverted jointly with the condition that the slip distribution, at the appropriate epochs, predicts the sparse data set. Consequently, these data place constraints on the spatial distribution of the principal slip distribution represented by the vectors *l*, but not on the time functions *V*.

As in section 5, we balance the weight put on each data set used in PCAIM by rescaling the uncertainties so that the weighted RMS of the residuals (or χ^2_{red}, equation (4)), computed for each data set separately, is equal to 1. Weighting is adjusted iteratively; generally only 1 or 2 iterations are necessary. Assessing the appropriate weighting to assign to a sparse data set, relative to the weight placed on fitting the *U* vectors is not
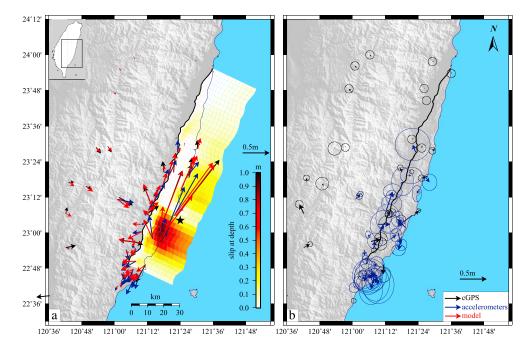

Figure 10. Coseismic slip distribution model of the 2003 M_w 6.8 Chengkung earthquake. (a) The grid shows slip on the fault inferred from the inversion of the static coseismic displacements determined at the cGPS and accelerometric stations, indicated by black and blue arrows, respectively. Predictions from our best fitting coseismic model are plotted in red. (b) Residuals between observed and predicted horizontal displacements. The black star indicates the epicenter of the Chengkung earthquake, and the black line represents the fault trace of the Longitudinal Valley Fault.
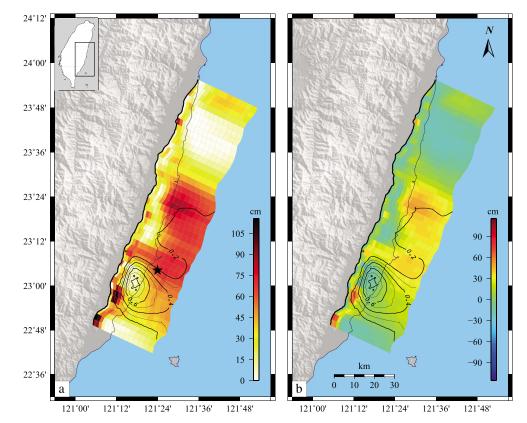
Figure 11. Postseismic slip distribution model following the M_w 6.8, Chengkung earthquake of 2003. (a) Cumulative slip on the LVF over the period between 11 December 2003 and 26 November 2010, determined from PCAIM inversion of cGPS and creepmeter time series, leveling data (from 1 September 2007 to 31/10/2010) and PS ALOS cumulative displacement between 29 January 2007 and 2 June 2010. The black star indicates the epicenter of the 2003 Chengkung earthquake. Black curves show the contour lines of the coseismic slip distribution model of the Chengkung earthquake (Figure 10). (b) Difference between postseismic slip and secular slip predicted from the secular model (Figure 7).

straightforward. For example, in the case of a data set consisting of cGPS and SAR data, the GPS time series should bring a stronger constraint, since they provide a daily, uncorrelated record of absolute position. However, through the PCAIM procedure, we reduce drastically the number of input parameters by applying an Singular Value Decomposition (SVD). Therefore, the ALOS data set becomes too predominant, whereas there is an inherent redundancy in the information provided by PS, directly correlated with the StaMPS procedure itself. As the data covariance is not an output of the StaMPS processing, to circumvent that issue, we arbitrarily penalize the ALOS data set by increasing estimated errors 10 times (Table 2). Other data uncertainties have been renormalized to get a χ^2_{red} of 1.

We perform separate inversions for the periods preceding and following the Chengkung earthquake. The two inversions are thus independent, and any similarity between these solutions has to come from the data rather than from the decomposition.

6.2. Postseismic Inversion

We model the time evolution of fault slip on the LVF over 7 years following the Chengkung earthquake using all the geodetic data and InSAR data available over that period. A PCA decomposition is applied to the cGPS and creepmeter stations time series. Based on the variation of the misfit as a function of the number of principal components, we determine that the first four components are significant (Figure S11 in the supporting information). These four components capture well the spatiotemporal variation of postseismic relaxation and the seasonal variations of surface displacement. The weight put on Laplacian smoothing and renormalization factors are listed in Table 2 along with the RMS values obtained from our inversion.

Figure 11 shows the slip distribution model over this time period. Temporal variation of slip at depth is discussed in more detail in section 7. The fit to the cumulative displacements measured at the cGPS stations is
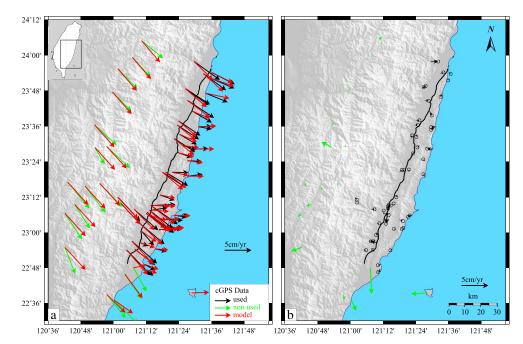
Figure 12. Postseismic slip distribution model, fit to geodetic data. (a) Comparison between observed and predicted horizontal displacement over the time period from 11 December 2003 to 26 November 2010. The reference frame is the Philippine Sea Plate, fixed. The cGPS data, which were used or not in the inversion, are plotted respectively as black and green arrows. Corresponding predictions of the postseismic slip model of 11 are displayed in red. (b) Residuals from the inversion with corresponding error ellipses. Same color coding as in Figure 12a.

presented in Figures 12 and S14 (in the supporting information), and the fit to the InSAR and leveling data is presented in Figures S15 and S16. Time variations of surface displacements predicted by the model are plotted in Figure 3 for cGPS and the creepmeter time series at a few sites surrounding the coseismic area. Other time series predictions can be found in Figures S1–S3. The principal slip distributions *l* and their associated time functions *V* are shown in Figures S12 and S13.

The spatial pattern of aseismic creep in the postseismic period (Figure 11a) turns out to be very similar to the secular pattern (Figure 7a) with enhanced slip of up to 72 cm surrounding the coseismic rupture (Figure 11b). According to this model (Figure 11b), afterslip over the 7 years following the Chengkung earthquake has released the cumulative moment of 1.53×10^{19} N m, about 0.8 times the coseismic moment.

6.3. Preseismic Slip Model

We also used the PCAIM procedure to analyze the temporal variation of fault creep before the 2003 earthquake, between January 1997 and December 2003. The spatial resolution is much worse than in the postseismic period, since only 20 continuous GPS stations are available for this time period and among them, only four stations have records before 2002. To improve the resolution power of the inversion, we augment the data set with the campaign GPS measurements, which were acquired between 1992 and 1999. These data are treated as sparse in the PCAIM inversion. Creepmeter time series have also been incorporated in this inversion since we have strain measurements across the fault back to 1998.

Variation of the total χ^2 in function of the number of principal components shows that only three components are significant (i.e., needed to reconstruct the original time series within uncertainties). Most of the signal is explained by the first component (Figure S11 in the supporting information), which is linear in time (Figure S17 in the supporting information). The weight put on Laplacian smoothing and renormalization factors are listed in Table 2, along with the RMS values obtained from our inversion. The principal slip distributions *l* and their associated time functions *V* are shown in Figures S18 and S17, respectively.

The distribution of slip rate averaged over the preseismic period is plotted in Figure 13. Fit to the mean surface velocities at the continuous GPS stations and GPS campaign sites is displayed in Figures 14 and S19 (in the supporting information). Time variations of surface displacements predicted by the model are plotted
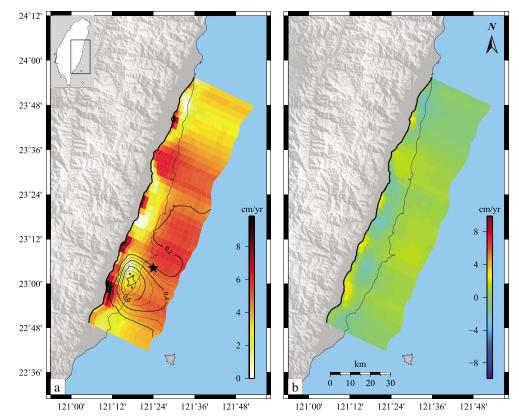
Figure 13. Preseismic slip distribution model. (a) Mean slip rate on the fault over the 1 January 1997 to 12 December 2003 period, inferred from PCAIM inversion of the campaign GPS data, the cGPS, and creepmeter time series. The black star indicates the epicenter of the 2003 Chengkung earthquake. Black curves are contour lines of the coseismic slip distribution model for the 2003 M_w 6.8 Chengkung Earthquake (Figure 10). (b) Difference between the preseismic slip rate and the secular slip rate predicted from the secular model (Figure 7).
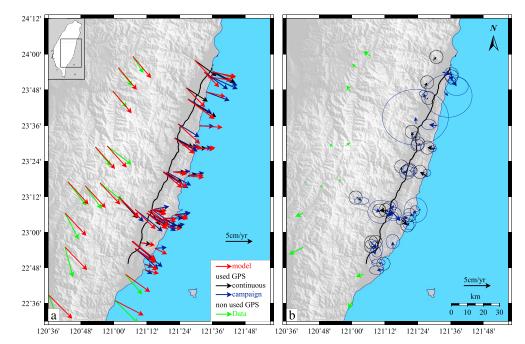
in Figure 3 at a few continuous GPS stations and for the creepmeter. Comparison of observed and predicted time series at other stations can be found in Figures S1–S3.
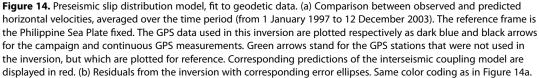
As Figure 13b emphasizes the preseismic model derived from the PCAIM procedure and the secular slip rate model are very similar. Differences between the two models are most likely related to the lower resolution of the time-dependent preseismic inversion. This modeling indicates that aseismic slip over the 7 years preceding the Chengkung earthquake was essentially steady state and released a cumulative moment of 3.86×10^{19} N m, which is about 2 times the coseismic moment released during the Chengkung earthquake.

7. Slip History on the LVF in the Chengkung Earthquake Area Over the 1997–2010 Period

It is now possible to describe the time evolution of slip on the LVF over the study period. We focus on the Chengkung earthquake area, where the temporal variations are the most noticeable. In fact, the rest of the fault does not exhibit detectable variations for the time periods considered. Also, in contrast to the northern portion of the LVF, this southern section is probably not influenced by the Ryukyu subduction zone.

Figure 15 provides a synthetic view of the time evolution of slip in the Chengkung earthquake area. The map view shows a close-up view of the distribution of interseismic creep rates, which was derived from the inversion of the secular surface strain rate (Figure 7a). We also show the time evolution of slip at a number of representative patches, retrieved from combining the source model of the earthquake with the PCAIM models for the preseismic and postseismic periods. The cumulative slip vector at each epoch is projected on the direction of the long-term slip vector predicted by the block motion of the Coastal Range relative to the Central Range. Our model indicates that over the 14 years between 1997 and 2010, this fault area has slipped by a total of 1 m to 1.5 m. This is approximately the cumulative slip for that period of time expected

Figure 14. Preseismic slip distribution model, fit to geodetic data. (a) Comparison between observed and predicted horizontal velocities, averaged over the time period (from 1 January 1997 to 12 December 2003). The reference frame is the Philippine Sea Plate fixed. The GPS data used in this inversion are plotted respectively as dark blue and black arrows for the campaign and continuous GPS measurements. Green arrows stand for the GPS stations that were not used in the inversion, but which are plotted for reference. Corresponding predictions of the interseismic coupling model are displayed in red. (b) Residuals from the inversion with corresponding error ellipses. Same color coding as in Figure 14a.

from the long-term oblique convergence between the Coastal Range and the Central Range. The results show that slip resulted from a combination of steady creep, unsteady creep, and seismic slip in proportions that vary in space.

Comparison of the secular pattern of creep rate with the slip contour lines of the coseismic rupture during the Chengkung earthquake clearly shows that the rupture extent coincides closely with an area that remained mostly locked in the interseismic period and relocked immediately after (Figures 7b and 5d). Time evolution of slip for patch 291 is instructive in that regard (Figure 15). This patch lies at a depth of about 15 km in the middle of the zone with peak seismic slip. According to our model, this patch slipped by about 0.8 m and relocked immediately after the earthquake. The earthquake nucleated at the edge of this locked zone (see epicenter in Figure 15), ruptured the entire locked patch, and did not propagate far into the surrounding creeping areas, except at depth where the overlap could be partially due to the smoothing induced by the regularization of our inversions, as Figure 5 illustrates, but not entirely. The rupture failed in particular to propagate across the shallow portion of the fault at a depth of less than about 7 km (see slip history at patch 301 in Figure 15), in agreement with the absence of surface ruptures observed in the field [*Lee et al.*, 2006] and the other source models of this earthquake [*Wu et al.*, 2006a; *Hu et al.*, 2007; *Wu and Wu*, 2007; *Mozziconacci et al.*, 2009].

The secular slip rate on the upper part of the fault, which is creeping in the interseismic period, as the InSAR and creepmeter measurements indicate, varies along strike (Figure 15). Patches 331 and 228 show similar behavior for the interseismic period: high creep rate was inferred (8.2 cm/yr for 331 and 6.7 cm/yr for 228), whereas patch 301 displays a smaller creep velocity (2.9 cm/yr), likely because it is in the stress shadow of the locked segment (see, for example, *Hetland and Simons* [2010] for a modeling study illustrating this effect). During coseismic, we estimate at patches 331 and 301, which correspond to the uppermost part of the fault, only a few centimeters of slip. On the contrary, we infer at patch 228, which stands at a 9 km depth, a coseismic jump of ∼ 20 cm. The creep rate increased abruptly right after the earthquake and then relaxed, leading to an approximately logarithmic increase of slip with time, but at different rates for the three patches. The maximum displacement is estimated at patch 228, where the slip rate after 7 years is 1.2 times higher than before December 2003. Patch 301 also slipped at faster rate (4.8 cm/year, i.e, 1.6 times faster),
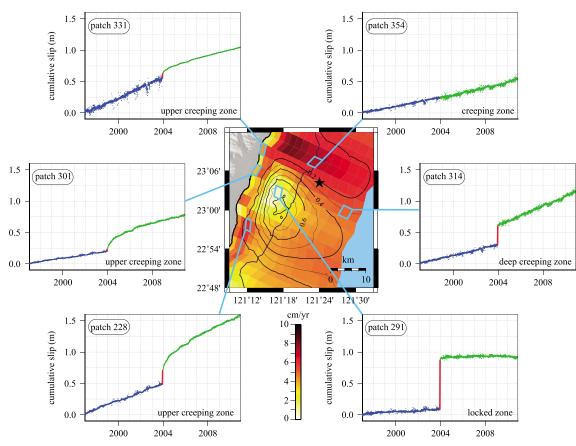
Figure 15. Slip at depth through time obtained from combining PCAIM inversions of preseismic and postseismic period and coseismic slip due to the Chengkung earthquake. Map view shows a close-up view of the secular slip rate distribution over the whole study period (see Figure 7a for location), with contour lines of the coseismic slip model (black lines) and epicenter (star) of the 2003 Chengkung earthquake. Graphs around the map view show the time evolution of slip at six patches along the direction of the slip vector predicted by the block motion of the Coastal Range relative to the Central Range. Patch 331, 301, and 228 sample the upper creeping zone. Patch 291 is characteristic of the zone which was locked before the Chengkung earthquake, slipped during the event, and relocked immediately after. Patches 314 and 354 illustrate the behavior of the deeper fault portion which is most poorly resolved.

but patch 331, on the contrary, underwent a decrease in slip velocity after the Chengkung earthquake (4.8 cm/yr).

Evidence for transient afterslip at depth below the rupture is less clear due to the poor resolution of the inversions. No transient is seen at patch 354, which seems to have been creeping at a nearly constant rate (3.3 cm/yr) throughout the study period. Patch 314, which according to our model was creeping in the pre-seismic period at 4.8 cm/yr, slipped during the Chengkung earthquake (0.3 m), and creeped more rapidly in the postseismic period (6.7 cm/year), but we do not observe the typical logarithmic behavior seen at shallower depth, suggesting a possible longer relaxation time. Nevertheless, it is hard to tell if this observation is really required by the data and warrants interpretation.

8. Discussion

8.1. Spatial Distribution of Seismic and Aseismic Creep, Role of the Lichi Mélange

The data set assembled in this study demonstrates that most of the southern portion of the LVF is creeping at the surface, though at a rate lower than the long-term slip rate required by the block motion of the Coastal Range with respect to the Central Range. By contrast, no surface creep is detected along the northern half of the LVF, which displays a high stress buildup (Figure 7b).

Comparison with surface geology supports earlier inferences [*Hsu et al.*, 2009a] that the Lichi Mélange could be responsible for promoting aseismic creep. This clay-rich formation, interpreted as a collision mélange [*Chang et al.*, 2000, 2001, 2009; *Huang et al.*, 2006, 2008], crops out in the Coastal Range and seems to fringe the creeping segment of LVF (Figure 2a). This formation does not extend along the northern segment of

the LVF, where only isolated outcrops have been interpreted to correspond to that particular formation [*Teng*, 1980]. Instead, fore-arc basin units (Fanshuliao and Paliwan formations) and volcanic arc products of the Tuluanshan formation crop out along the surface trace of the LVF. The southern segment of the fault can nevertheless also produce large seismic events, as the Chengkung earthquake demonstrates. However, the rupture occurred in the 10–20 km depth range and did not reach the surface. Our interseismic model indicates that the earthquake actually ruptured a fault patch that was locked before 2003 and relocked immediately after and is surrounded by a zone that is dominantly creeping. The Lichi Mélange is an important factor controlling along-strike variations of creep rate, but whether it is through the intrinsic properties of its dominant minerals or whether it is related to the hydrological properties of this formation is unclear at this point. It is noteworthy that the seismic crisis of 1951, with its four $M_w > 6.8$ shocks, did produce surface ruptures along the northern portion of the LVF but also along the Chihshang segment in the south during a subevent with magnitude similar to the 2003 event [*Shyu et al.*, 2007; *Lee et al.*, 2008]. It thus looks like the ability of the shallow creeping segment to impede seismic rupture propagation varies. This might be due to changes of the fault frictional properties or to different rupture geometry and dynamics during the 2003 earthquake and the 1951 subevent on the Chihshang segment.

8.2. Seismic and Aseismic Slip Budget, Implication for the Return Period of $M_w > 6.8$ Earthquakes on the LVF

Our modeling results allow estimation of the relative proportion of seismic and aseismic slip on the LVF and draw inferences regarding the return period of large earthquakes in this area. The reader should be aware of the large uncertainties involved in this discussion. It is particularly difficult to formally take into account all the possible sources of errors due not only to the measurement uncertainties but also to the modeling assumptions. For example, it is probably not correct to assume that the CeR and CoR blocks can be considered rigid in the long run nor to neglect the strain associated with the complicated junction with the Ryuku subduction zone north of the Longitudinal Valley. However, it is still worth illustrating the kind of questions which can be addressed based on the modeling attempt presented in this study.

Interseismic strain implies a rate of accumulation of slip potency ($SP_{deficit}$), or, equivalently, moment deficit, which can be computed from integrating the slip rate deficit over the locked fault zones (section 4.3 and 4.2):

$$M_{0_{deficit}} = \mu \cdot SP_{deficit} = \mu \sum_i V_i \cdot ISC_i \cdot S_i, \tag{9}$$

where S_i is the area of the subfault, V_i is the long-term slip rate inferred in section 4.2 based on the CeR/CoR pole, and the interseismic coupling coefficient ISC_i quantifies the degree of locking defined in section 4.3. We estimated the moment deficit rate to be $2.77 \times 10^{18} N\,m\,yr^{-1}$ for the whole LVF. If we consider the southern section only, with the upper boundary defined as the transition between the creeping section and the locked zone in the north (Figure 7b), we obtain a value of $1.12 \times 10^{18} N\,m\,yr^{-1}$ (Table 3). Then, given the cumulative moment released by the coseismic slip and the following afterslip (Table 3) inferred in this study, the return period of earthquakes similar the Chengkung earthquake can be estimated from the equation

$$T = \frac{M_{0_{coseismic}} + M_{0_{postseismic}}}{M_{0_{deficit}}}. \tag{10}$$

Based on this equation, we get a return period of ~13 years if we considered the whole LVF, and ~34 years for the southern section. These estimates seem reasonable given that five earthquakes with $M_w \geq 6.8$ occurred over the last century [*Shyu et al.*, 2007; *Chung et al.*, 2008; *Lee et al.*, 2008; *Wu et al.*, 2008b]. Therefore, this analysis shows there is no need for larger or more frequent earthquakes than those known historically to balance the deficit of slip due to the pattern of locking on the LVF in the interseismic period.

It is then instructive to compare our estimate of the return period of $M_w > 6.8$ earthquakes on the LVF with the frequency-magnitude distribution of instrumental earthquakes in the area, displayed in Figure 16. For that purpose we used the 1991–2010 seismicity catalog from *Wu et al.* [2008a], selecting events lying on the southern half portion of the LVF, where our model is best constrained (see seismicity map in Figure S12). Seismic data follows the Gutenberg-Richter law:

$$\log_{10}(N(m > M_w)) = a - bM_w, \tag{11}$$

Table 3. Moments and Moment Magnitudes Inferred From Inversion Models

	Models	Moment	Equivalent M_w
ISC (deficit)[a]	all LVF	3.31×10^{18} N m yr^{-1}	6.28
	south LVF	1.35×10^{18} N m yr^{-1}	6.02
Preseismic[a]	all LVF	7.69×10^{18} N m yr^{-1}	6.52
	south LVF	5.20×10^{18} N m yr^{-1}	6.41
Coseismic	all LVF	2.50×10^{19} N m	6.86
	south LVF	2.26×10^{19} N m	6.83
Postseismic[b]	all LVF	1.92×10^{19} N m	6.79
	south LVF	2.34×10^{19} N m	6.85

[a]Moments and moment magnitudes values are cumulated over 1 year.
[b]Cumulative value after ~7 years, for the afterslip only, i.e., minus the secular model.

where N is the number of events which have a moment magnitude greater or equal to M_w; a and b are constants with a typical value of 1 for the b parameter in seismically active regions. We divided the data set into three time periods: from 1 January 1991 to 31 December 2009 (all catalog), from 1 January 1991 to 9 December 2003 (before the 2003 Chengkung earthquake), and from 10 December 2003 and thereafter. Above their magnitude of completeness (which is about 1.8), those three subsets of the main catalog return a similar b value of 0.95 for the complete data set and 0.90 and 0.94 for seismicity selected before and after the main shock, respectively (Figure 16). The return period of a Chengkung-type earthquake inferred from this study can be plotted in this diagram (Figure 16). It shows a nice consistency with the instrumental catalog, since the Gutenberg-Richter distribution defined above yields a return period of ~24 years for a $M_w = 6.8$ earthquake if we were considering the whole LVF and ~36 years if we only select earthquakes in the southern section of the LVF (Figure 16).
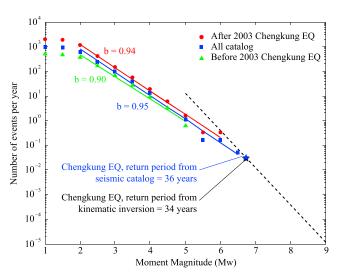

Figure 16. Frequency-magnitude distribution of seismicity from 1991 to 2010 on the Longitudinal Valley, using the catalog from *Wu et al.* [2008a], for the southern portion of the fault (see S21a in the supporting information for location). The graph shows, in ordinate, the number of events with moment magnitude equal or larger than a given value reported in abscissa. We divided the catalog into three time periods: in blue from 1991 to 2010 (all catalog), in green from 1991 to 9 December 2003 (before the 2003 Chenkung earthquake), and in red from 10 December 2003 and thereafter. Lines are Gutenberg-Richter distribution computed for magnitude $M_w \geq 2$. Returned b value are respectively 0.95 for the all catalog, 0.90 before the Chengkung earthquake, and 0.94 for seismicity selected after the main shock. The black star shows the return period computed from this study for Chengkung-type earthquake ($M_w = 6.8$) from balancing the seismic and aseismic slip budget on the LVF. The blue star highlights the prediction from the seismic catalog. The dashed line shows the return period of the maximum magnitude earthquakes, when its magnitude is varied, so that the interseismic deficit slip is balanced by seismic slip resulting from all the events defining the Gutenberg-Richter distribution.

We can also estimate the fraction of slip potency (or, equivalently, release moment), which results from aseismic (α), or seismic (γ) slip over the long-term average, assuming that known seismicity is representative of the long-term behavior. The fraction of aseismic slip is

$$\alpha = \frac{T \cdot \sum_i V_i \cdot (1 - \mathrm{ISC}_i) \cdot S_i + M_{0_{\text{postseismic}}} / \mu}{T \cdot \sum_i V_i \cdot S_i}. \tag{12}$$

This calculation tends to provide an overestimate, as it assumes that all of the measured geodetic strain results from aseismic creep, except for the effect of the Chengkung earthquake. We estimated this fraction to be about 77% for the whole LVF. If we focus on the southern portion, where the model is more reliable (not biased by interseismic strain associated with the Ryuku subduction zone), we get an even larger value of 92%. This estimate is probably representative of the long-term average, as the study period is long enough compared to the return period of large earthquakes. The average interseismic creep pattern is reasonably well constrained, and the contribution of transient aseismic creep due to afterslip following the Chenkgung earthquake is only a small fraction of the total budget. This estimate has a large uncertainty, in relation with uncertainties on our slip models, among other factors.

The fraction of seismic slip is

$$\gamma = \frac{\sum M_{0_i}}{\mu \cdot t_{\text{cat}} \cdot \sum_i V_i \cdot S_i}, \tag{13}$$

where the numerator accounts for the moment released by all earthquakes on the LVF during the study period t_{cat}. This quantity can be bracketed if we consider on one end only the Chengkung earthquake, which unambiguously occurred on the LVF, and on the other end assume that all the earthquakes recorded in the study area over the study period occurred on the LVF and add their scalar seismic moments by extrapolating the number of earthquakes with magnitude below the detection threshold based on the Gutenberg-Richter law (Figure 16). We thus assess the numerator to be between 1.87×10^{19} and 2.77×10^{19} for the entire fault, and between 1.68×10^{19} and 2.40×10^{19} for the southern segment. The corresponding fraction of seismic slip is then between 14% and 21% if all the LVF is considered. It is estimated to be between 20% and 28%, accounting for the southern section only, where most of the aftershocks occur (see Figure S21). This estimate is not necessarily representative of the long-term average, given that the earthquake catalog does not cover several earthquake cycles; thus, the moment released by the largest earthquakes on the LVF in the long run is poorly constrained. Despite all the uncertainties in these estimates, it is interesting to note that the slip budget approximately closes.

9. Conclusion

This study demonstrates that a large fraction (80–90%) of the long-term slip budget on the LVF in the 0–26 km seismogenic depth range (as defined by local seismicity) is actually the result of aseismic creep. The spatial pattern of aseismic creep on the LVF is very heterogeneous, showing both along-dip and along-strike variations. Creep is observed at the surface along the southern portion of the LVF, where it seems to correlate with Lichi Mélange. The M_w 6.8 Chenkgung earthquake of 2003 ruptured a 12.5 km $\times$ 15.8 km patch that had remained locked in the interseismic period; it extends at a depth between 8 and 20 km. The earthquake seems to have nucleated at the boundary of the locked zone, where stress builds up in the interseismic period. Slip then propagated through the locked patch but failed to rupture the surrounding creeping areas (Figures 7, 10, and 13). Afterslip, due to enhanced creep in the immediate vicinity of the rupture, released a moment equivalent to 0.8 times the seismic moment of the earthquake and decreased approximately logarithmically with time. This time evolution is consistent with the time evolution of afterslip excepted from velocity-strengthening friction [*Marone et al.*, 1991; *Perfettini and Avouac*, 2004]. These observations suggest that the location and the extent of seismic asperities are largely controlled by permanent rheological properties of the fault zone, which, in the present case, seems to relate to lithology.

To first order, this simple picture is consistent with theoretical models of the seismic cycle based on lateral and depth variation of frictional properties of faults [e.g., *Lapusta et al.*, 2000; *Rice and Ben-Zion*, 1996; *Scholz*, 1998]. In those models, aseismic slip occurs in velocity-strengthening areas during the interseismic period until instability occurs at the boundary between velocity-strengthening and velocity-weakening zones, leading to the nucleation of seismic events that rupture previously locked velocity-weakening zones.

Depending on the size and on the frictional properties of the velocity-strengthening zones, seismic events are able to propagate through the creeping sections or are stopped by them [*Kaneko et al.*, 2010]. Then, relaxation of coseismic stress results in acceleration of aseismic slip in the velocity-strengthening areas until it comes back to interseismic rates. Our study thus confirms the suggestion that aseismic patches tend to play a key role in arresting seismic ruptures, presumably because aseismic creep prevents stress buildup and because the presumably velocity-strengthening rheology absorbs energy during seismic rupture propagation [*Kaneko et al.*, 2010]. The LVF thus stands out as a candidate example where a dynamic model of the seismic cycle could be designed and calibrated from comparison with geodetic and seismic data as has been done on the Parkfield segment of the San Andreas Fault [*Barbot et al.*, 2012].

References

Ader, T., et al. (2012), Convergence rate across the Nepal Himalaya and interseismic coupling on the main Himalayan thrust: Implications for seismic hazard, *J. Geophys. Res.*, *117*, B04403, doi:10.1029/2011JB009071.

Angelier, J., H. T. Chu, and J. C. Lee (1997), Shear concentration in a collision zone: Kinematics of the Chihshang fault as revealed by outcrop-scale quantification of active faulting, Longitudinal Valley, eastern Taiwan, *Tectonophysics*, *274*(1–3), 117–143.

Barbot, S., N. Lapusta, and J. P. Avouac (2012), Under the hood of the earthquake machine: Toward predictive modeling of the seismic cycle, *Science*, *336*(6082), 707–710.

Burgmann, R., D. Schmidt, R. M. Nadeau, M. d'Alessio, E. Fielding, D. Manaker, T. V. McEvilly, and M. H. Murray (2000), Earthquake potential along the Northern Hayward Fault, California, *Science*, *289*(5482), 1178–1182.

Champenois, J. (2011), Caractérisation des déformations tectoniques inter-sismiques de l'île de Taiwan par interférométrie radar, PhD thesis, Paris Est.

Champenois, J., B. Fruneau, E. Pathier, B. Deffontaines, K. C. Lin, and J. C. Hu (2012), Monitoring of active tectonic deformations in the longitudinal valley (eastern Taiwan) using persistent scatterer InSAR method with ALOS PALSAR data, *Earth Planet. Sci. Lett.*, *337*, 144–155.

Chang, C. P., J. Angelier, and C. Y. Huang (2000), Origin and evolution of a mélange: The active plate boundary and suture zone of the Longitudinal Valley, Taiwan, *Tectonophysics*, *325*(1–2), 43–62.

Chang, C. P., J. Angelier, C. Y. Huang, and C. S. Liu (2001), Structural evolution and significance of a mélange in a collision belt: The Lichi Mélange and the Taiwan arc-continent collision, *Geol. Mag.*, *138*(6), 633–651.

Chang, S. H., W. H. Wang, and J. C. Lee (2009), Modelling temporal variation of surface creep on the Chihshang fault in eastern Taiwan with velocity-strengthening friction, *Geophys. J. Int.*, *176*(2), 601–613.

Chen, H. Y., S. B. Yu, L. C. Kuo, and C. C. Liu (2006), Coseismic and postseismic surface displacements of the 10 December 2003 (m-w 6.5) Chengkung, eastern Taiwan, earthquake, *Earth Planets Space*, *58*(1), 5–21.

Chen, H. Y., Y. J. Hsu, J. C. Lee, S. B. Yu, L. C. Kuo, Y. L. Jiang, C. C. Liu, and C. S. Tsai (2009), Coseismic displacements and slip distribution from GPS and leveling observations for the 2006 Peinan earthquake (m-w 6.1) in southeastern Taiwan, *Earth Planets Space*, *61*(3), 299–318.

Chen, H. Y., J. C. Lee, H. Tung, S. B. Yu, Y. J. Hsu, and H. Lee (2012), Determination of vertical velocity field of southernmost longitudinal valley in eastern Taiwan: A joint analysis of leveling and GPS measurements, *Terr. Atmos. Oceanic Sci.*, *23*(4), 355–376.

Cheng, L.-W., J.-C. Lee, J.-C. Hu, and H.-Y. Chen (2009), Coseismic and postseismic slip distribution of the 2003 mw = 6.5 Chengkung earthquake in eastern Taiwan: Elastic modeling from inversion of GPS data, *Tectonophysics*, *466*(3–4), 335–343.

Ching, K. E., R. J. Rau, and Y. H. Zeng (2007), Coseismic source model of the 2003 M_w 6.8 Chengkung earthquake, Taiwan, determined from GPS measurements, *J. Geophys. Res.*, *112*, B06422, doi:10.1029/2006JB004439.

Ching, K. E., M. L. Hsieh, K. M. Johnson, K. H. Chen, R. J. Rau, and M. Yang (2011), Modern vertical deformation rates and mountain building in Taiwan from precise leveling and continuous GPS observations, 2000-2008, *J. Geophys. Res.*, *116*, B08406, doi:10.1029/2011JB008242.

Chlieh, M., J. P. Avouac, K. Sieh, D. H. Natawidjaja, and J. Galetzka (2008), Heterogeneous coupling of the Sumatran megathrust constrained by geodetic and paleogeodetic measurements, *J. Geophys. Res.*, *113*, B05305, doi:10.1029/2007JB004981.

Chuang, R. Y., M. M. Miller, Y. G. Chen, H. Y. Chen, J. B. H. Shyu, S. B. Yu, C. M. Rubin, K. Sieh, and L. H. Chung (2012), Interseismic deformation and earthquake hazard along the southernmost Longitudinal Valley Fault, eastern Taiwan, *Bull. Seismol. Soc. Am.*, *102*(4), 1569–1582.

Chung, L. H., Y. G. Chen, Y. M. Wu, J. B. H. Shyu, Y. T. Kuo, and Y. N. N. Lin (2008), Seismogenic faults along the major suture of the plate boundary deduced by dislocation modeling of coseismic displacements of the 1951 m7.3 Hualien-Taitung earthquake sequence in eastern Taiwan, *Earth Planet. Sci. Lett.*, *269*(3–4), 415–425.

Copley, A., J. Hollingsworth, and E. Bergman (2012), Constraints on fault and lithosphere rheology from the coseismic slip and postseismic afterslip of the 2006 m(w)7.0 Mozambique earthquake, *J. Geophys. Res.*, *117*, B03404, doi:10.1029/2011JB008580.

Cross, R. S., and J. T. Freymueller (2007), Plate coupling variation and block translation in the Andreanof segment of the Aleutian arc determined by subduction zone modeling using GPS data, *Geophys. Res. Lett.*, *34*, L06304, doi:10.1029/2006GL028970.

DeMets, C., R. G. Gordon, and D. F. Argus (2011), Geologically current plate motions (vol 181, pg 1, 2010), *Geophys. J. Int.*, *187*(1), 538–538.

Evans, E. L., J. P. Loveless, and B. J. Meade (2012), Geodetic constraints on San Francisco Bay Area fault slip rates and potential seismogenic asperities on the partially creeping Hayward fault, *J. Geophys. Res.*, *117*, B03410, doi:10.1029/2011JB008398.

Ferretti, A., C. Prati, and F. Rocca (2001), Permanent scatterers in SAR interferometry, *IEEE Trans. Geosci. Remote Sens.*, *39*(1), 8–20.

Fournier, T. J., and J. T. Freymueller (2007), Transition from locked to creeping subduction in the Shumagin region, Alaska, *Geophys. Res. Lett.*, *34*, L06303, doi:10.1029/2006GL029073.

Freymueller, J. T., S. C. Cohen, and H. J. Fletcher (2000), Spatial variations in present-day deformation, Kenai peninsula, Alaska, and their implications, *J. Geophys. Res.*, *105*(B4), 8079–8101.

Hanks, T. C., and H. Kanamori (1979), Moment magnitude scale, *J. Geophys. Res.*, *84*(NB5), 2348–2350.

Heki, K., S. Miyazaki, and H. Tsuji (1997), Silent fault slip following an interplate thrust earthquake at the Japan trench, *Nature*, *386*(6625), 595–598.

Hetland, E., and M. Simons (2010), Post-seismic and interseismic fault creep II: Transient creep and interseismic stress shadows on megathrusts, *Geophys. J. Int.*, *181*(1), 99–112.

Hooper, A., P. Segall, and H. Zebker (2007), Persistent scatterer interferometric synthetic aperture radar for crustal deformation analysis, with application to Volcan Alcedo, Galapagos, *J. Geophys. Res.*, *112*, B07407, doi:10.1029/2006JB004763.

Hsu, L., and R. Burgmann (2006), Surface creep along the Longitudinal Valley Fault, Taiwan from InSAR measurements, *Geophys. Res. Lett.*, *33*, L06312, doi:10.1029/2005GL024624.

Hsu, Y. J., M. Simons, S. B. Yu, L. C. Kuo, and H. Y. Chen (2003), A two-dimensional dislocation model for interseismic deformation of the Taiwan mountain belt, *Earth Planet. Sci. Lett.*, *211*(3–4), 287–294.

Hsu, Y. J., M. Simons, J. P. Avouac, J. Galetzka, K. Sieh, M. Chlieh, D. Natawidjaja, L. Prawirodirdjo, and Y. Bock (2006), Frictional afterslip following the 2005 Nias-Simeulue earthquake, Sumatra, *Science*, *312*(5782), 1921–1926.

Hsu, Y. J., J. P. Avouac, S. B. Yu, C. H. Chang, Y. M. Wu, and J. Woessner (2009a), Spatio-temporal slip, and stress level on the faults within the western foothills of Taiwan: Implications for fault frictional properties, *Pure Appl. Geophys.*, *166*(10–11), 1853–1884.

Hsu, Y. J., S. B. Yu, and H. Y. Chen (2009b), Coseismic and postseismic deformation associated with the 2003 Chengkung, Taiwan, earthquake, *Geophys. J. Int.*, *176*(2), 420–430.

Hu, J. C., et al. (2007), Coseismic deformation revealed by inversion of strong motion and GPS data: The 2003 Chengkung earthquake in eastern Taiwan, *Geophys. J. Int.*, *169*(2), 667–674.

Huang, B. S., W. G. Huang, Y. L. Huang, L. C. Kuo, K. C. Chen, and J. Angelier (2009), Complex fault rupture during the 2003 Chengkung, Taiwan earthquake sequence from dense seismic array and GPS observations, *Tectonophysics*, *466*(3–4), 184–204.

Huang, C. Y., C. W. Chien, B. C. Yao, and C. P. Chang (2008), The Lichi Mélange: A collision melange formation along early arcward back-thrusts during fore-arc basin closure, Taiwan arc-continent collision, in *Formation and Applications of the Sedimentary Record in Arc Collision Zones, Geological Society of America Special Papers*, vol. 436, edited by A. E. Draut, P. D. Clift, and D. W. Scholl, pp. 127–154, Geol. Soc. Am. Inc., Boulder, Colo.

Huang, M. H., J. C. Hu, C. S. Hsieh, K. E. Ching, R. J. Rau, E. Pathier, B. Fruneau, and B. Deffontaines (2006), A growing structure near the deformation front in SW Taiwan as deduced from SAR interferometry and geodetic observation, *Geophys. Res. Lett.*, *33*, L12305, doi:10.1029/2005GL025613.

Huang, W. J., K. M. Johnson, J. Fukuda, and S. B. Yu (2010), Insights into active tectonics of eastern Taiwan from analyses of geodetic and geologic data, *J. Geophys. Res.*, *115*, B03413, doi:10.1029/2008JB006208.

Jolivet, R., C. Lasserre, M. P. Doin, S. Guillaso, G. Peltzer, R. Dailu, J. Sun, Z. K. Shen, and X. Xu (2012), Shallow creep on the Haiyuan Fault (Gansu, China) revealed by SAR Interferometry, *J. Geophys. Res.*, *117*, B06401, doi:10.1029/2011JB008732.

Kaneko, Y., J.-P. Avouac, and N. Lapusta (2010), Towards inferring earthquake patterns from geodetic observations of interseismic coupling, *Nat. Geosci.*, *3*, 363–369.

Kaneko, Y., Y. Fialko, D. T. Sandwell, X. Tong, and M. Furuya (2013), Interseismic deformation and creep along the central section of the North Anatolian Fault (Turkey): InSAR observations and implications for rate-and-state friction properties, *J. Geophys. Res. Solid Earth*, *118*, 316–331, doi:10.1029/2012JB009661.

Kositsky, A. P., and J. P. Avouac (2010), Inverting geodetic time series with a principal component Analysis-based Inversion Method, *J. Geophys. Res.*, *115*, B03401, doi:10.1029/2009JB006535.

Kuo, L. (2008), Standardized automatic processing procedures of GPS continuous data (in chinese), *Tech. Rep.* Institute of Earth Sciences, Academia Sinica, Taiwan.

Kuochen, H., Y. M. Wu, Y. G. Chen, and R. Y. Chen (2007), 2003 mw6.8 Chengkung earthquake and its related seismogenic structures, *J. Asian Earth Sci.*, *31*(3), 332–339.

Langbein, J., and H. Johnson (1997), Correlated errors in geodetic time series: Implications for time-dependent deformation, *J. Geophys. Res.*, *102*(B1), 591–603.

Lapusta, N., J. R. Rice, Y. Ben-Zion, and G. T. Zheng (2000), Elastodynamic analysis for slow tectonic loading with spontaneous rupture episodes on faults with rate-and-state dependent friction, *J. Geophys. Res.*, *105*(B10), 23,765–23,789.

Lee, J. C., and J. Angelier (1993), Location of active deformation and geodetic data analyses: An example of the Longitudinal Valley Fault, Taiwan, *Bull. Soc. Geol. Fr.*, *164*, 533–570.

Lee, J. C., J. Angelier, H. T. Chu, S. B. Yu, and J. C. Hu (1998), Plate-boundary strain partitioning along the sinistral collision suture of the Philippine and Eurasian plates: Analysis of geodetic data and geological observation in southeastern Taiwan, *Tectonics*, *17*(6), 159–181.

Lee, J.-C., J. Fu-Shu, C. Hao-Tsu, J. Angelier, and H. Jyr-Ching (2000), A rod-type creepmeter for measurement of displacement in active fault zone, *Earth Planets Space*, *52*(5), 321–328.

Lee, J. C., J. Angelier, H. T. Chu, J. C. Hu, and F. S. Jeng (2001), Continuous monitoring of an active fault in a plate suture zone: A creepmeter study of the Chihshang fault, eastern Taiwan, *Tectonophysics*, *333*(1–2), 219–240.

Lee, J. C., J. Angelier, H. T. Chu, J. C. Hu, F. S. Jeng, and R. J. Rau (2003), Active fault creep variations at Chihshang, Taiwan, revealed by creep meter monitoring, 1998–2001, *J. Geophys. Res.*, *108*(B11), 2528, doi:10.1029/2003JB002394.

Lee, J. C., J. Angelier, H. T. Chu, J. C. Hu, and F. S. Jeng (2005), Monitoring active fault creep as a tool in seismic hazard mitigation. Insights from creepmeter study at Chihshang, Taiwan, *C. R. Geosci.*, *337*(13), 1200–1207.

Lee, J. C., H. T. Chu, J. Angelier, J. C. Hu, H. Y. Chen, and S. B. Yu (2006), Quantitative analysis of surface coseismic faulting and postseismic creep accompanying the 2003, m-w = 6.5, Chengkung earthquake in eastern Taiwan, *J. Geophys. Res.*, *111*, B02405, doi:10.1029/2005JB003612.

Lee, Y. H., G. T. Chen, R. J. Rau, and K. E. Ching (2008), Coseismic displacement and tectonic implication of 1951 Longitudinal Valley earthquake sequence, eastern Taiwan, *J. Geophys. Res.*, *113*, B04305, doi:10.1029/2007JB005180.

Lin, Y.-n. N., A. P. Kositsky, and J.-P. Avouac (2010), PCAIM joint inversion of InSAR and ground-based geodetic time series: Application to monitoring magmatic inflation beneath the Long Valley Caldera, *Geophys. Res. Lett.*, *37*, L23301, doi:10.1029/2010GL045769.

Lohman, R. B. (2004), The inversion of geodetic data for earthquake parameters, PhD thesis, California Institute of Technology.

Loveless, J. P., and B. J. Meade (2011), Spatial correlation of interseismic coupling and coseismic rupture extent of the 2011 $M_w = 9.0$ Tohoku-oki earthquake, *Geophys. Res. Lett.*, *38*, L17306, doi:10.1029/2011GL048561.

Ma, K.-F., C.-T. Lee, Y.-B. Tsai, T.-C. Shin, and J. Mori (1999), The Chi-Chi, Taiwan earthquake: Large surface displacements on an inland thrust fault, *Eos Trans. AGU*, *80*(50), 605–611.

Malavieille, J., et al. (2002), Arc-continent collision in Taiwan: New marine observations and tectonic evolution, in *Geology and Geophysics of an Arc-Continent Collision, Taiwan*, edited by T. B. Byrne and C.-S. Liu, pp. 187–211, Geological Society of America Special Paper 358, Boulder, Colo.

Marone, C. J., C. H. Scholz, and R. Bilham (1991), On the mechanics of earthquake afterslip, *J. Geophys. Res.*, *96*(B5), 8441–8452.

McCaffrey, R. (2005), Block kinematics of the Pacific–North America plate boundary in the southwestern United States from inversion of GPS, seismological, and geologic data, *J. Geophys. Res.*, *110*, B07401, doi:10.1029/2004JB003307.

Meade, B. J., and B. H. Hager (2005), Block models of crustal motion in southern California constrained by GPS measurements, *J. Geophys. Res.*, *110*, B03403, doi:10.1029/2004JB003209.

Miyazaki, S., J. J. McGuire, and P. Segall (2011), Seismic and aseismic fault slip before and during the 2011 off the Pacific coast of Tohoku earthquake, *Earth Planets Space*, *63*(7), 637–642.

Mozziconacci, L., B. Delouis, J. Angelier, J. C. Hu, and B. S. Huang (2009), Slip distribution on a thrust fault at a plate boundary: The 2003 Chengkung earthquake, Taiwan, *Geophys. J. Int.*, *177*(2), 609–623.

Murray, J. R., P. Segall, P. Cervelli, W. Prescott, and J. Svarc (2001), Inversion of GPS data for spatially variable slip-rate on the San Andreas Fault near Parkfield, CA, *Geophys. Res. Lett.*, *28*(2), 359–362.

Okada, Y. (1985), Surface deformation to shear and tensile faults in a half space, *Bull. Seismol. Soc. Am.*, *75*(4), 1135–1154.

Ozawa, S., T. Nishimura, H. Munekane, H. Suito, T. Kobayashi, M. Tobita, and T. Imakiire (2012), Preceding, coseismic, and postseismic slips of the 2011 Tohoku earthquake, Japan, *J. Geophys. Res.*, *117*, B07404, doi:10.1029/2011JB009120.

Perfettini, H., and J. R. Avouac (2004), Stress transfer and strain rate variations during the seismic cycle, *J. Geophys. Res.*, *109*, B06402, doi:10.1029/2003JB002917.

Perfettini, H., et al. (2010), Seismic and aseismic slip on the central Peru megathrust, *Nature*, *465*(7294), 78–81.

Peyret, M., S. Dominguez, R. Cattin, J. Champenois, M. Leroy, and A. Zajac (2011), Present-day interseismic surface deformation along the Longitudinal Valley, eastern Taiwan, from a PS-InSAR analysis of the ERS satellite archives, *J. Geophys. Res.*, *116*, B03402, doi:10.1029/2010JB007898.

Pritchard, M. E., and M. Simons (2006), An aseismic slip pulse in northern Chile and along-strike variations in seismogenic behavior, *J. Geophys. Res.*, *111*, B08405, doi:10.1029/2006JB004258.

Rice, J. R., and Y. Ben-Zion (1996), Slip complexity in earthquake fault models, *Proc. Nat. Acad. Sci. U.S.A.*, *93*(9), 3811–3818.

Rosen, P. A., S. Hensley, G. Peltzer, and M. Simons (2004), Updated repeat orbit interferometry package released, *Eos Trans. AGU*, *85*(5), 47, doi:10.1029/2004EO050004.

Savage, J. C. (1983), A dislocation model of strain accumulation and release at a subduction zone, *J. Geophys. Res.*, *88*(NB6), 4984–4996.

Savage, J. C. (2007), Postseismic relaxation associated with transient creep rheology, *J. Geophys. Res.*, *112*, B05412, doi:10.1029/2006JB004688.

Scholz, C. H. (1998), Earthquakes and friction laws, *Nature*, *391*, 37–42.

Sella, G. F., T. H. Dixon, and A. L. Mao (2002), REVEL: A model for Recent plate velocities from space geodesy, *J. Geophys. Res.*, *107*(B4), ETG 11-1–ETG 11-30, doi:10.1029/2000JB000033.

Shyu, J. B. H., K. Sieh, Y.-G. Chen, and C.-S. Liu (2005), Neotectonic architecture of Taiwan and its implications for future large earthquakes, *J. Geophys. Res.*, *110*, B08402, doi:10.1029/2004JB003251.

Shyu, J. B. H., K. Sieh, J. P. Avouac, W. S. Chen, and Y. G. Chen (2006), Millennial slip rate of the Longitudinal Valley fault from river terraces: Implications for convergence across the active suture of eastern Taiwan, *J. Geophys. Res.*, *111*, B08403, doi:10.1029/2005JB003971.

Shyu, J. B. H., L. H. Chung, Y. G. Chen, J. C. Lee, and K. Sieh (2007), Re-evaluation of the surface ruptures of the November 1951 earthquake series in eastern Taiwan, and its neotectonic implications, *J. Asian Earth Sci.*, *31*(3), 317–331.

Teng, L. S. (1980), On the origin and tectonic significance of the Lichi formation, northern Coastal Range, eastern Taiwan, *Ti-Chih*, *2*, 51–62.

Titus, S. J., C. DeMets, and B. Tikoff (2006), Thirty-five-year creep rates for the creeping segment of the San Andreas Fault and the effects of the 2004 Parkfield earthquake: Constraints from alignment arrays, continuous global positioning system, and creepmeters, *Bull. Seismol. Soc. Am.*, *96*(4), S250–S268.

Wallace, L. M., J. Beavan, R. McCaffrey, and D. Darby (2004), Subduction zone coupling and tectonic block rotations in the North Island, New Zealand, *J. Geophys. Res.*, *109*, B12406, doi:10.1029/2004JB003241.

Williams, S. D. P. (2003), The effect of coloured noise on the uncertainties of rates estimated from geodetic time series, *J. Geod.*, *76*(9–10), 483–494.

Wiseman, K., P. Banerjee, K. Sieh, R. Bürgmann, and D. H. Natawidjaja (2011), Another potential source of destructive earthquakes and tsunami offshore of Sumatra, *Geophys. Res. Lett.*, *38*, L10311, doi:10.1029/2011GL047226.

Wu, Y. M., and C. F. Wu (2007), Approximate recovery of coseismic deformation from Taiwan strong-motion records, *J. Seismolog.*, *11*(2), 159–170.

Wu, Y. M., Y. G. Chen, T. C. Shin, H. Kuochen, C. S. Hou, J. C. Hu, C. H. Chang, C. F. Wu, and T. L. Teng (2006a), Coseismic versus interseismic ground deformations, fault rupture inversion and segmentation revealed by 2003 mw 6.8 Chengkung earthquake in eastern Taiwan, *Geophys. Res. Lett.*, *33*, L02312, doi:10.1029/2005GL024711.

Wu, Y. M., Y. G. Chen, C. H. Chang, L. H. Chung, T. L. Teng, F. T. Wu, and C. F. Wu (2006b), Seismogenic structure in a tectonic suture zone: With new constraints from 2006 mw6.1 Taitung earthquake, *Geophys. Res. Lett.*, *33*, L22305, doi:10.1029/2006GL027572.

Wu, Y.-M., C.-H. Chang, L. Zhao, J. B. H. Shyu, Y.-G. Chen, K. Sieh, and J.-P. Avouac (2007), Seismic tomography of Taiwan: Improved constraints from a dense network of strong motion stations, *J. Geophys. Res.*, *112*, B08312, doi:10.1029/2007JB004983.

Wu, Y. M., C. H. Chang, L. Zhao, T. L. Teng, and M. Nakamura (2008a), A comprehensive relocation of earthquakes in Taiwan from 1991 to 2005, *Bull. Seismol. Soc. Am.*, *98*(3), 1471–1481.

Wu, Y. M., C. C. Chen, L. Zhao, and C. H. Chang (2008b), Seismicity characteristics before the 2003 Chengkung, Taiwan, earthquake, *Tectonophysics*, *457*(3–4), 177–182.

Yu, S. B., and L. C. Kuo (2001), Present-day crustal motion along the Longitudinal Valley Fault, eastern Taiwan, *Tectonophysics*, *333*(1–2), 199–217.

Yu, S. B., H. Y. Chen, and L. C. Kuo (1997), Velocity field of GPS stations in the Taiwan area, *Tectonophysics*, *274*(1–3), 41–59.

Zhang, J., Y. Bock, H. Johnson, P. Fang, S. Williams, J. Genrich, S. Wdowinski, and J. Behr (1997), Southern California permanent GPS geodetic array: Error analysis of daily position estimates and site velocities, *J. Geophys. Res.*, *102*(B8), 18,035–18,055.